Experimental determination of the dispersion relation of magnetosonic waves

S. N. Walker,[1] M. A. Balikhin,[1] D. R. Shklyar,[2] K. H. Yearby,[1] P. Canu,[3]

C. M. Carr,[4] and I. Dandouras[5,6]

Corresponding author: S. N. Walker, Department of Automatic Control and Systems Engineering, University of Sheffield, Sheffield, UK. (simon.walker@sheffield.ac.uk)

[1]Department of Automatic Control and Systems Engineering, University of Sheffield, Sheffield, UK.

[2]Space Research Institute, Russian Academy of Sciences, Moscow, Russia.

[3]LPP/CNRS, Palaiseau, France.

[4]Blackett Laboratory, Imperial College London, London, UK.

[5]UPS-OMP, IRAP, Toulouse, France.

[6]CNRS, IRAP, Toulouse, France.

Abstract. Magnetosonic waves are commonly observed in the vicinity of the terrestrial magnetic equator. It has been proposed that within this region they may interact with radiation belt electrons, accelerating some to high energies. These wave-particle interactions depend upon the characteristic properties of the wave mode. Hence determination of the wave properties is a fundamental part of understanding these interaction processes. Using data collected during the Cluster Inner Magnetosphere Campaign, this paper identifies an occurrence of magnetosonic waves, discusses their generation and propagation properties from a theoretical perspective, and utilises multispacecraft measurements to experimentally determine their dispersion relation. Their experimental dispersion is found to be in accordance with that based on cold plasma theory.

1. Introduction

Electromagnetic equatorial noise, or magnetosonic waves (MSW) as they are more commonly referred to, consist of intense electromagnetic emissions that occur close to the magnetic equator of the terrestrial magnetosphere. MSW have been suggested to play an important role in the local acceleration of radiation belt electrons from 10 keV to relativistic energies via resonant interactions [*Gurnett*, 1976; *Horne et al.*, 2007]. First principles based models of the particle environment of the radiation belts include terms such as wave-particle interactions in the form of energy, pitch angle, and mixed diffusion coefficients. The derivation of these terms is strongly dependent upon the assumed wave propagation characteristics. Based on the cold plasma description of MSW [*Mourenas et al.*, 2013] demonstrated that the pitch-angle scattering and energy diffusion rates of high energy electrons decrease sharply as the wave normal angle approaches 90° and that these rates also depend inversely on the width of the wave normal distribution. In addition, *Albert* [2008] reported that the scattering rates also depended upon the rate of change of wave normal angle with frequency ($d\theta/d\omega$). Since the dispersion relation of MSW and resonance condition essentially define the relationship between the resonant energy and either the pitch angle (for a given wave normal angle) or wave normal angle (for a given energy and pitch angle) any deviation from the cold plasma dispersion would result in a marked change in the energy/pitchangle ranges that are affected by these waves [*Mourenas et al.*, 2013]. Using such parameters, physics based first principles models (e.g. VERB [*Shprits et al.*, 2008, 2009]) are able to estimate electron fluxes throughout the radiation belt region.

MSW were first reported by *Russell et al.* [1970]. Using data from OGO-3, these authors described observations of magnetic fluctuations in the frequency range between the proton gyrofrequency (Ω_p) and an upper limit around half of the lower hybrid resonance (LHR) frequency (ω_{LH}). The waves were found to occur within 2° of the magnetic equator at distances in the range $L = 3 - 5$. Their propagation characteristics showed that the waves possessed a high degree of elliptical polarisation, with a wave normal angle almost perpendicular to the external magnetic, and the wave magnetic perturbations directed parallel to the external magnetic field. Electric field observations by *Gurnett* [1976] from the IMP-6 and Hawkeye 1 satellites revealed that these emissions, whose frequency was typically in the range 50-200 Hz, possess a complex frequency structure with the large spectral peaks observed around the proton gyroharmonic frequencies possessing a finer substructure characterised by frequencies of $\Omega_p/8$ and $\Omega_p/2$ i.e. heavy ion gyrogrequencies. The dominant oscillations occurred at harmonics of the proton gyrofrequency. *Perraut et al.* [1982]; *Laakso et al.* [1990]; *Boardsen et al.* [1992]; *Kasahara et al.* [1994]; *André et al.* [2002] and *Balikhin et al.* [2015] also showed further evidence for the harmonic structure of these waves and investigated their morphology. More recent studies by [*Chen et al.*, 2011] and *Němec et al.* [2005] demonstrated that the magnetosonic wave instability could operate over a broad range of frequencies from 5 to $40\Omega_p$. This multiharmonic spectral structure is indicative of interactions at some characteristic resonance frequency. *Horne et al.* [2007] suggested that the cyclotron resonances tend to occur at high (MeV) energies and therefore unlikely to play a major role in the scattering of electrons whilst the Landau resonance may operate over a wide range of energies from below 100 keV. An alternate mechanism [*Russell et al.*, 1970; *Shprits*, 2009] suggests that electrons may also be scattered by bounce resonant interactions [*Roberts and Schulz*, 1968]. Recent reports by *Fu et al.* [2014], *Boardsen et al.* [2014], and *Němec et al.* [2015] have shown the existence of periodic, rising tone MSW using data from THEMIS, VAP, and Cluster respectively. The cause of this periodicity is still unknown, though it may be linked to the occurrence of ULF magnetic field pulsations.

Perraut et al. [1982] were able to correlate their observations of MSW with the appearance of peaks in the energy spectra of 90° pitch angle protons (ring-like ion distributions), suggesting this as the source of free energy for the growth of these waves. These authors used this theoretical model to investigate the dispersion characteristics of the observed waves. The dispersion obtained was characterised by multiple branches at frequencies $\omega \sim n\Omega_p$, reducing to the cold plasma dispersion ($\omega \sim k_\perp V_A$) in the case of a vanishing ring density. Maximum growth occurred at wave numbers that corresponded to the crossover points between the cold dispersion and that resulting from the ring distribution. The frequency range of instability has been shown to depend upon the ratio of the Alfvén velocity (V_A) and the velocity of the proton ring (V_R) [*Perraut et al.*, 1982; *Korth et al.*, 1984; *Boardsen et al.*, 1992; *Horne et al.*, 2000; *Chen et al.*, 2010; *Ma et al.*, 2014]. The ring distribution may provide the source of free energy for the growth of MSW when $0.5 < V_R/V_A < 2$. This ratio also controls the range of frequencies that are unstable. High values of V_R/V_A result in MSW at low proton gyroharmonic frequencies whilst lower ratios yield waves at high (>20) harmonics. Using sets of parameters based on measured ring-type ion distributions *Balikhin et al.* [2015] was able to recreate the frequency spectrum of the observed wave emissions. *Korth et al.* [1983, 1984] also proposed a second possible generation mechanism based on the occurrence of a sharp gradient in the observed plasma pressure as a free energy source for instabilities such as a drift wave instability. *Meredith et al.* [2008] and *Chen et al.* [2011] showed that the region where proton ring distributions were observed was generally consistent with the distribution of MSW. *Thomsen et al.* [2011] analysed the occurrence of ring-like distributions at Geosynchronous Orbit (GSO), concluding that these distributions were most likely to occur in the afternoon sector during periods of low Kp and small Dst and that there appeared to be a discrepancy between the occurrence of ring-like proton distributions and the occurrence of MSW. It was concluded that storms, due to either coronal mass ejections or high speed streams, actually suppressed the occurrence of these distributions.

Since these waves propagate, on average, in a direction nearly perpendicular to the external magnetic field they are confined to the equatorial region, enabling potential azimuthal guiding by the plasmasphere, as well as radial translation [*Bortnik and Thorne*, 2010]. These effects were considered by *Chen and Thorne* [2012] who investigated the extent to which magnetosonic waves may propagate azimuthally. Waves trapped within the plasmasphere may migrate indefinitely until damped. Waves of plasmaspheric origin that are not trapped within the plasmasphere may propagate up to 4hrs in MLT whilst those originating outside the plasmapause may migrate up to 7hrs MLT, possibly explaining the discrepancy in the distributions of proton rings and magnetosonic waves at geosynchronous orbit [*Thomsen et al.*, 2011]. *Perraut et al.* [1982] described the propagation of these waves from the source region to the point of observation and the fact that they would retain their harmonic structure from the source region, i.e. the spacing of the harmonic bands reflects the magnetic field of the source region which may not be the same as that of the local field at the location of observation. Using multipoint measurements, *Santolík* *et al.* [2002] showed spectral differences between observations made by two of the Cluster satellites. These authors suggested that this may result from either two different source regions, different regions of the same extended source region, or from the propagation of the waves. Whilst these emissions are observed to occur within a few degrees of the magnetic equator, detailed analysis by *Santolík et al.* [2002] and *Němec et al.* [2005] have shown that they tend to reach a maximum intensity at a latitude 2-3° above the equator, a point corresponding to the minimum magnetic field strength along the magnetic field line.

2. Cluster Inner Magnetosphere Campaign

The goal of the Cluster Inner Magnetosphere Campaign was to study the role of magnetosonic waves and chorus emissions in the process energization of electrons within the radiation belts. This program of observations took place between July and October 2013. During this period, Cluster employed a "100 km formation" which resulted in intersatellite separations of around 30 km for the pair C3 and C4 with C1 typically 300-400 km distant. Cluster 2 was situated around 5000 km from the other 3 satellites. Since the main observations are targeted at the plasma wave environment, new modes of operation for the Cluster Wave Experiment Consortium (WEC) [*Pedersen et al.*, 1997] were devised, tested, and implemented within the Digital Wave Processor (DWP) [*Woolliscroft et al.*, 1997], the WEC control instrument. These modes, referred to as BM2, enable the possibility of collecting high resolution (equivalent to burst mode science) data from the Electric fields and Waves (EFW) [*Gustafsson et al.*, 1997] and the Spatio-Temporal Analysis of Field Fluctuations (STAFF) search coil magnetometer [*Cornilleau-Wehrlin et al.*, 1997] together with the possibility of timesharing telemetry resources between Wide-band

(WBD) [*Gurnett et al.*, 1997] waveforms, decimated by a factor 3 or 4, and spectra from the WHISPER relaxation sounder [*Décréau et al.*, 1997]. This mode operated in addition to periods of normal Cluster burst science mode telemetry (BM1) to increase the number of high resolution observations available in the vicinity of the magnetic equator.

3. Data Source

The data presented in this paper were collected on July 6^{th}, 2013, during a period using the burst science telemetry mode (BM1) on all Cluster satellites. This mode of operation provided electric field measurement from EFW instrument and magnetic field oscillations from the STAFF search coil magnetometer with a sampling resolution of 450 Hz together with Fluxgate Magnetometer (FGM) [*Balogh et al.*, 1997] measurements of the background magnetic field at a resolution of 67 Hz. The ion data used in this study were collected by the Cluster Ion Spectrometer (CIS) instrument[*Reme et al.*, 1997].

During the period 1832-1857 UT on July 6^{th}, 2013 the Cluster spacecraft were passing through the inner magnetosphere at a radial distance of the order of 3.8-4.2 R_E on the dayside at a local time 1330-1250, and crossed the magnetic equator at around 1844 UT, travelling north to south between magnetic latitudes of 1.9° and -2.3°. The four panels in Figure 1 show the location of the Cluster satellites (lower right) and the relative separations of the Cluster quartet (in the GSE frame). Satellites C3 and C4 were separated by around 60 km and so appear on top of each other at the scales shown in Figure 1. The separation distances between C3/C4 and C1 was around 1000 km whilst C2 was around 4300 km distant. As a result, C3 and C4 observed almost identical patterns of wave emissions, C1 observed similar overall structure whilst the observations of C2 are completely different owing to its different location. The external magnetic field during this period varies from 487 nT at the beginning of the period to 287 nT at the end, implying the proton gyrofrequency gradually changing from 7.4 Hz to 4.4 Hz and the lower hybrid frequency from 318 to 187 Hz. The electron density, estimated from WHISPER electric field spectra was in the range 15-19 cm^{-3}. Based on these density values and the assumption of a proton only plasma, the Alfvén velocity varies in the range 2600-1600kms^{-1}. These values represent an upper limit to the value of V_A which reduces when heavy ions are included. The level of geomagnetic disturbance during the period under study was moderate. At the beginning of July 6^{th}, the Dst index increased during the early hours of July 6^{th} from around 0 to -60 nT and maximising at ~ -79 nT around 19 UT before decreasing over the following two days.

4. Observations

4.1. Wave spectrum

As mentioned in Section 3, during this period both the STAFF search coil magnetometer sampled the plasma wave environment at a resolution of 450 Hz. Figure 2 shows the dynamic spectra measured by the search coil magnetometers on satellites 3 (panel a) and 4 (panel b). The black lines indicate the 15, 20, 25, and 30^{th} harmonics of the local proton gyrofrequency. Both Cluster 3 an 4 observe a set of banded emissions beginning around 18:40 and continuing until the end of the BM1 operations at 18:57. Initially, the emissions are observed in the frequency range 130-170 Hz, corresponding to the 21^{st}-30^{th} gyro-harmonics. As the Cluster satellites continue to travel southward, the amplitude of the waves increases, maximising at a latitude of around -1° before decreasing until the end of observations. Thus the amplitudes are asymmetrically distributed around the equator in line with results reported by *Santolík et al.* [2002] (based on the T89 magnetic field model

[*Tsyganenko*, 1989]).During this period, the external magnetic field weakens as evidenced by the decrease in the gyrofrequency harmonics. At the same time, the emission frequency of the waves drops, mirroring the change observed on the gyrofrequency harmonics. This frequency change is evidence that the waves are observed in their source region.

Figure 3 shows averaged spectra of the Cluster 4 STAFF search coil Bx (GSE) measurements centred at (top to bottom)18:43, 18:46, 18:51, and 18:56. Each spectrum is the average of 9 1024 point Fourier spectra. The vertical dotted black lines mark the $14^{th} - 30^{th}$ harmonics of the local proton gryofrequency. It is noticeable that two types of emission can be seen in Figures 2 and 3. The first corresponds to the higher frequency emissions seen in the top three plots of Figure 3. These high frequency emissions occur close to harmonics of the local proton gyrofrequency in the range $20\Omega_p < \omega < 30\Omega_p$ and as the magnetic field decreases so does the frequency of emission. The position of the peaks relative to the gyrofrequency harmonics changes with time. In panel (a) the majority of the spectral peaks are observed just below the gyroharmonics whilst in panel (b), corresponding to the time around the magnetic field line minimum, the peaks are at the gyro frequencies. As the spacecraft moves away from the field line minimum the frequency relative to the gyroharmonic falls.

Figure 4 shows the FFT spectrum of emissions between 18:48:40 and 18:49:20 UT calculated by averaging nine 2048 point FFTs. The external magnetic field in this period varied from 339-335 nT (Ω_p changes from 5.2-5.14 Hz). The format is the same as that in Figure 3. During this period, emission lines are observed in the frequency range from $14\Omega_p$ to $29\Omega_p$. The position of the emission with respect to the harmonic frequency varies with harmonic number. At the low frequency end of the spectrum e.g. harmonics 14-18, the emissions occur at the exact frequency of the gyroharmonic whereas at higher frequencies the emissions lie slightly below the harmonic. In the case of the 23 and 24 harmonics the frequency difference is around 1.1 Hz. The other noticeable feature in this Figure is that most harmonics (except those mentioned above) exhibit multiple peaks. This could indicate the existence of further interactions with heavier ions such as He^+, He^{2+}, or O^+ ions. This harmonic structure implies that resonant interactions have a dominant role in the generation of these waves. This topic will be investigated further in a later paper.

The second type of emissions is seen in Figures 2 and 3 (panel d), measured around 18:56 UT. These emissions are observed in the frequency range 10-16Ω_p. and occur between the local gyroharmonics. Their frequency spacing is of the order of 4.3 Hz and analysis of spectra recorded after 18:56 UT (not shown). These emissions are monotonic, their frequency does not depend upon the local gyrofrequency. Emissions such as these are more typical of those discussed by other authors when they refer to magnetosonic waves or equatorial noise [e.g. *Santolík et al.*, 2002]. The reason for their constant frequency is that these waves were generated at some other location and have propagated to the location in which they are observed. Since the frequency spacing of these emissions is lower than the local proton gyrofrequency these emissions are generated in a region of lower magnetic field strength (∼282 nT) most probably at a greater radial distance, and have propagated to the point at which they were observed. Unfortunately, these emissions were not observed on C3 due to a mode change a few seconds before.

4.2. Ion distributions

As noted in Section 1, the occurrence of magnetosonic waves are associated with ring-like ion distributions [*Perraut et al.*, 1982; *Chen et al.*, 2011]. Figure 5 shows the 1D ion distributions measured by CIS-CODIF instrument onboard Cluster 4. It should be noted that these observations are heavily contaminated due to the passage of the satellite through the radiation belts. In spite of this, evidence for the existence of a ring-like distribution is still very strong. The top panel shows the pitch-angle distribution of protons in the energy range 7-38.5 keV. These distributions are strongly peaked at pitch angles around 90°, indicative of a ring-like distribution. During the period in which the waves are observed the particle flux observed increased, with the highest fluxes observed after 1850UT corresponding to the period when emissions at high harmonics vanish whilst those at lower frequencies become less intense. This change in the distribution is also evident in the bottom panel which shows the particle count rate as a function of energy and time. The highest count rates are observed at energies above 10 keV, maximising in the region of 20-30 keV. This is the energy of the proton ring and corresponds to a velocity of the order V_r= 2000-2400 kms^{-1}. This velocity is greater than the Alfvén velocity (calculated in Section 3). Thus, the ring distribution could provide the free energy to enable the growth of the MSW since the energy of the ring distribution exceeds the Alfvén energy [*Korth et al.*, 1984]. Moving towards lower energies there is a distinct minimum in the energy just below the ring particles that occurs at an energy of around 7 keV. This energy, referred to as the dip energy/dip velocity (V_{dip}) [e.g. *Chen et al.*, 2011], corresponds to a velocity of around 1100 kms^{-1}. Thus, for velocities in the range $V_{dip} < v_\perp < V_r$ the proton distribution has a positive gradient ($\partial f / \partial v_\perp > 0$).

Using the results of the theoretical analysis performed by *Chen et al.* [2010], it is possible to estimate the frequencies at which the instability occurs and wave growth is observed. The blue curve in Figure 6 shows the approximate perpendicular velocity in terms of the Alfvén velocity that corresponds to peak wave growth as a function of the harmonic resonance. Also plotted (black lines) are V_A (dotted), V_{dip} (dashed), and V_r (dash-dotted). Thus it would be expected that there should be emission bands in the range 8-29Ω_p since $V_{dip} < v_\perp < V_r$. The wave spectra, measured in the period 1844:45 to 1845:15 is shown in red. It is clear from this Figure that all harmonics at which waves were observed correspond to perpendicular velocities in the range $V_{dip} < v_\perp < V_r$, inline with results reported by *Chen et al.* [2010]. These results are consistent with the general trend reported by *Ma et al.* [2014]. From Figure 6 , the value of $V_r/V_A \sim 1.02$ which would imply that the unstable wave frequencies would be expected at frequencies around the mid-range of possible harmonics, exactly as was observed and shown in this figure.

4.3. Wave Properties

In order to establish the propagation mode of the waves that were observed during this period the basic properties of these emissions were investigated based on the measurements from Cluster 4. In the previous Section it was shown that the bands of emission at higher frequencies typically occurred at or just below harmonics of the proton gyrofrequency. In this section, the wave polarisation and propagation characteristics are investigated.

The wave properties for the period 18:47:00-18:47:20 UT, based on the STAFF search coil measurements, are shown in Figure 7. During this period, the proton gyrofrequency was 5.32 Hz. These results are based on the use of a Morlet wavelet transform to extract the frequency information from the waveform and Singular Valued Decomposition [*Santolik et al.*, 2003] to compute the eigenvectors and eigenvalues of the complex spectral matrix. It should be noted that the signal after 18:47:19 UT is superposed with a broad band signal arising from some local interference whose effects can be seen most clearly on the three lower panels.

The top panel in Figure 7 shows a spectrogram of the emissions in the frequency range 70-170 Hz. The banded nature of the emissions can be clearly seen and their amplitudes are not constant but vary independently. In the panels below data is only plotted when the trace of the spectral matrix exceeds a level of 1×10^{-7} nT^2Hz^{-1}.

The ellipticity of the banded emissions, defined as the ratio of the intermediate eigenvalue to the maximum eigenvalue i.e. e_{int}/e_{max} is plotted in the second panel. A value of unity implies circular polarisation, whilst zero indicates linear. As is evident from this panel, the majority of emissions are highly elliptical with eigenvalue ratios typically $e_{int}/e_{max} < 0.1$.

The third panel displays the propagation angle of the waves with respect to the external magnetic field (obtained from FGM measurements). The distribution of k-direction is strongly peaked in the region of $\theta_{Bk} \sim 90°$ indicating almost perpendicular propagation of the wave. Figure 8 shows the distribution of $\mathbf{k}$ with respect to the external magnetic field direction in more detail. The X axis shows the angle between the wave vector and the external magnetic field (θ_{Bk}), using a bin size of 0.5°. The Y axis represents the normalised distribution of occurrence. An offset of 0.06 has been added to separate the distributions at different frequencies, the horizontal dashed line (of the same colour) representing the baseline Y=0 for the distribution. The frequency of each distribution is indicated to the right of the plot. Since the frequency decreases slowly over the ~20 second time period over which this analysis was performed, adjacent frequency bins have been averaged. The vertical dashed line indicates an angle $\theta_{Bk} = 90°$ whilst the dash-dotted lines mark angles of $\theta_{Bk} = 88.5$ and $\theta_{Bk} = 91.5°$. These plots show that the majority of the propagation angles occur in the range 87-93°. There appears to be two basic types of distribution. The first show a peak at $\theta_{Bk} = 90°$, indicating that the waves propagate perpendicularly to the external magnetic field. Such distributions are observed for waves of frequency 160.5, 150.5, 109.5, 107.5, and 92.5Hz. The second type of distribution exhibits a number of peaks in the angular distribution, indicating a preference for almost perpendicular propagation e.g. the distributions for frequencies 155.5, 113.5, 97.5, and 86.5Hz. Typically, the peaks occur within 2° of perpendicular, a value in line with that often quoted in discussions of the propagation of magnetosonic waves.

Finally, the fourth panel of Figure 7 displays the angle between the eigenvector of the magnetic field oscillations that corresponds to the maximum eigenvalue i.e. the direction of the principle axis of the polarisation ellipsoid and the direction of the external magnetic field. The distribution is centred on the direction antiparallel to the external magnetic field implying that the oscillations of the wave magnetic field occur in the direction parallel to the external magnetic field.

In summary, the banded emissions observed by the Cluster 4 STAFF search coil magnetometer during the period 18:47:00-18:47:20 UT are consistent with whistler mode waves propagating almost perpendicular to the eternal magnetic field since they are highly elliptical in nature and the wave magnetic field oscillates parallel to the external field. Thus these emissions are examples of magnetosonic waves (equatorial noise). This conclusion is further strengthened in the next sections by the determination of the dispersion relation of the observed waves and its comparison to dispersion relations derived theoretically.

5. Experimental Determination of the Dispersion Relation

The wave vector ($\mathbf{k}$) of a wave is a vector quantity whose direction corresponds to the wave propagation direction and whose magnitude is related to the wavelength (λ) of the wave ($|\mathbf{k}| = 2\pi/\lambda$). Determination of the wave vector is important when considering the propagation of waves within the plasma environment as well as their interaction with the local particle populations for which they provide a medium for the transfer of energy between the particle populations via either current or resonant instabilities.

Experimental determination of the wave vector has only been possible since the advent of multispacecraft missions and the possibility of making simultaneous measurements at two or more closely spaced points in space. Depending upon the type of data sets available, there are a number of different methods such as **k**-filtering/wave telescope [*Pinçon and Lefeuvre*, 1992], and phase differencing [*Balikhin and Gedalin*, 1993; *Balikhin et al.*, 1997a; *Chisham et al.*, 1999] that may be employed. These methods, which were compared in *Walker et al.* [2004], are based on the fact that a comparison of the simultaneous multipoint measurements will show differences in the phase of the wave at the different measurement locations. These differences may then be used to determine the **k**-vector of the wave. In the present paper, the phase differencing methodology is employed.

Following *Balikhin et al.* [1997b] and *Balikhin et al.* [2001] the basic assumption behind the phase differencing method is that the measured wave field may be represented by the superposition of plane waves as shown by equation (1)

$$\mathbf{B}(\mathbf{r}, t) = \Sigma_\omega \mathbf{B}_\omega \exp[i(\mathbf{k} \cdot \mathbf{r} - \omega t)] + cc \tag{1}$$

where $\mathbf{B}_\omega$ is the wave amplitude at frequency ω, $\mathbf{k}$ is the wave vector (k-vector), $\mathbf{r}$ is the separation vector between the location of the two (or more) simultaneous measurements, and *cc* represents the complex conjugate term. A comparison of observations from two closely spaced locations will display a difference in the phases of the measurements of the wave. This phase shift $\Delta\psi$ is proportional to the component of the wave vector $\mathbf{k}$ projected along the measurement separation direction $\mathbf{r}$ (assuming that there is only one wave vector $\mathbf{k}$ for any frequency ω) and is given by (2).

$$\begin{aligned}\Delta\psi(\omega) &= \mathbf{k}(\omega)\cdot\mathbf{r} + 2n\pi \\ &= \|\mathbf{k}\|\|\mathbf{r}\|\cos(\theta_{kr}) + 2n\pi \qquad (2)\end{aligned}$$

where θ_{kr} is the angle between the wave vector $\mathbf{k}$ and the satellite separation vector $\mathbf{r}$ and n is an integer value. Since the phase difference between the two signals can only be determined in the range $-\pi < \Delta\psi < \pi$, a family of periodic solutions is possible, resulting in a phase ambiguity of $2n\pi$. Thus, in order to determine the correct value of $k_{\mathbf{r}}$ it is necessary to determine the correct value of n.

The phase differencing method may be applied to scalar measurements or single components of a vector quantity and results in a measurement of the component of the wave vector projected along the measurement separation vector. If measurements are available from four (or more) closely spaced, non-coplanar locations it is possible to determine the projection of the wave vector along three independent directions and hence determine the complete wave vector [*Balikhin et al.*, 2003]. However, if measurements from only two locations are available the size of k_r can be estimated but not it's direction and so another method is required to determine the direction of $\mathbf{k}$. One such method that may be used with magnetic field data is to calculate the eigenvalues and eigenvectors of the magnetic field covariance matrix. Provided that the ratio of the intermediate to minimum eigenvalues is large (typically a factor 10, i.e. the wave is not linearly polarised) then the minimum variance direction is well defined and represents the direction of wave propagation. Thus, knowledge of the direction together with the magnitude of k-vector projected along the measurement separation vector enables the full wave k-vector to be determined.

The phase differencing method was applied to measurements from the spacecraft Cluster 3 and 4 during the interval 18:47:13-18:47:16.5 UT on July 6^{th}, 2013. This period corresponds to a time when the emissions are observed from the 14^{th}-29^{th} proton gyroharmonic as seen in Figure 2. Figure 9 shows the $\omega - \mathbf{k}$ histogram of the variation in the phase difference measured between satellites C3 and C4. The left hand panel shows the phase differences recorded in the Bx component whilst that on the right shows the phase differences recorded in the Bz component. These plots show that in the frequency range 70-105 Hz there are emissions occurring at discrete frequency bands at around 77, 81, 87, 92, 98, 103 Hz. These frequencies correspond to the 14-19 harmonics of the proton gyrofrequency. At each of these frequencies there is a well defined maximum in the phase difference between the two signals detected on satellites C3 and C4. The reason for two peaks at each frequency is due to the $2n\pi$ ambiguity factor when determining the phase difference (equation 2). Knowledge of the satellite separation distance enables the values of phase difference to be converted into spatial measurements of the projection of the wave vector along the satellite separation direction and so the histogram represents the dispersion relation of the observed waves. It is clearly seen from Figure 9 that there is a linear feature running diagonally up and right to the top right corner of each panel. This line is a representation of the dispersion of the observed waves.

The features observed by satellites C3 and C4 are highly coherent due to their small separation in comparison with the coherency length of the waves. This cannot be said for the observations by Cluster 1, whilst Cluster 2 is in a completely different plasma location and does not see this banded structures at all. It is, therefore, not possible to use the phase differencing technique to determine the dispersion relations between other pairs of satellites in the Cluster quartet and hence compute the full k-vector. In order to find the direction of the wave k-vector another method is required. Since the above analysis is based on magnetic field measurements it is possible to obtain the direction of $\mathbf{k}$ by calculating the eigenvalues and corresponding eigenvectors of the magnetic field co-variance matrix. The analysis period (18:47:13-18:47:16.5 UT) was divided into a number of segments, each typically 0.25 seconds, and the eigenvalues and vectors were calculated. The direction of $\mathbf{k}$ was taken as the average of the minimum variance directions for which the corresponding ratio of the intermediate to minimum eigenvalues $\lambda_{int}/\lambda_{min} > 50$. This criteria ensures that the minimum variance direction is well defined. This direction, together with the projections of $\mathbf{k}$ along the satellite separation vector were used to compute the k-vector of the wave.

However, this still leaves the problem of resolving the ambiguity factor $2n\pi$ in the determination of the phase difference between the two signals. There are two scenarios for which the determination of n is reasonably straight forward. The first is for low frequency signals, i.e. those whose wavelength is much greater than the separation of the two measurement points in which case n would probably be zero and the phase difference could actually be computed directly from the waveforms [e.g. *Balikhin et al.*, 1997c]. The second scenario involves the comparison of isolated wave packets whose waveforms are virtually identical in both signals [e.g. *Balikhin et al.*, 2005]. Neither of these methods could be applied to the current case in question since the observed waves consist of a superposition of waves with a number of discrete frequencies and variable amplitudes. This fact also rules out the possibility of determining n from the shape of sequences of wave packets since they are just too irregular [*Walker and Moiseenko*, 2013]. Therefore, the only way to determine n is to compare the experimental dispersion with one determined from theory and match the two by changing the value of n.

6. Theoretical insight into the propagation of MSW

To get some insight into the properties of MSW it is instructive to consider the theoretical derivation of their dispersion relation, growth rate and propagation direction based on the local ion distribution. The contribution of the ions to the growth rate of MSW is investigated based on an approach first proposed about fifty years ago [*Dawson*, 1961; *O'Neil*, 1965] and has since been used for many studies of wave-particle interactions in the magnetosphere. This approach assumes the magnetospheric plasma is composed of two parts: a "cold" bulk population of electrons and ions that determines the plasma dispersion relation, and low-density suprathermal populations of electrons and ions which participate in resonant interactions with the waves and are responsible for wave growth or damping. If the wave growth (or damping) rate is less than the inverse nonlinear time of resonant interaction, the resonant particle distribution function can be found using the adiabatic approximation with respect to the wave amplitude, i.e. neglecting the amplitude variation during the time of resonant interaction.

6.1. Dispersion relation and polarization of magnetosonic waves below ω_{LH}

The electric field of a plane wave can be written as

$$\mathcal{E} = \mathrm{Re}\{\mathbf{a}Ee^{i(\mathbf{kr}-\omega t)}\} \tag{3}$$

where E is the complex wave amplitude and **a** is the complex polarization vector. In the reference frame in which the ambient magnetic field $\mathbf{B_0}$ is directed along the z-axis and the wave propagation vector ($\mathbf{k}$) lies in the (x,z) plane, the dielectric tensor of a cold plasma has the form [*Ginzburg and Rukhadze*, 1972]:

$$\varepsilon_{ij}(\omega) = \begin{pmatrix} \varepsilon_1 & i\varepsilon_2 & 0 \\ -i\varepsilon_2 & \varepsilon_1 & 0 \\ 0 & 0 & \varepsilon_3 \end{pmatrix} \tag{4}$$

In a cold, magnetized plasma, there is only one wave mode that propagates in the frequency range above proton cyclotron frequency Ω_p. This mode is right-hand polarized. The characteristics of this mode depend on both the wave frequency and the propagation angle θ between $\mathbf{k}$ and $\mathbf{B_0}$. In the case when the electron plasma frequency ω_p is larger than electron cyclotron frequency ω_c, this mode extends up to the frequency $\omega_c \cos\theta$. Another characteristic frequency, the so called lower hybrid resonance frequency, is defined as

$$\omega_{LH}^2 = \frac{1}{M_{eff}} \frac{\omega_p^2 \omega_c^2}{\omega_p^2 + \omega_c^2} \tag{5}$$

where effective ion mass M_{eff} is

$$\frac{1}{M_{eff}} = \frac{m_e}{n_e} \sum_{ions} \frac{n_i}{m_i} \tag{6}$$

Above this frequency, the wave propagation angle lies inside the resonance cone θ_R determined by the relation

$$\omega^2 = \omega_{LH}^2 + \omega_c^2 \cos^2\theta_R$$

At the resonance cone the wave refractive index $N = kc/\omega$ tends to infinity. Waves with frequencies above ω_{LH} are known as whistler-mode waves, whilst waves with frequencies close to the LHR frequency are often referred to as lower hybrid waves.

Below the LHR frequency, the propagation angle is arbitrary, including $\theta = \pi/2$. In this frequency range the propagating right-hand polarized waves are often termed magnetosonic waves.

For waves in the frequency range

$$\Omega_p \ll \omega \lesssim \omega_{LH} \ll \omega_c$$

and assuming $\omega_p \gg \omega_c$ the real part of the quantities $\varepsilon_1,\ \varepsilon_2,$ and ε_3 can be approximated by

$$\varepsilon_1 \simeq \frac{\omega_p^2 + \omega_c^2}{\omega_c^2}\left(1 - \frac{\omega_{LH}^2}{\omega^2}\right) \ ; \quad \varepsilon_2 \simeq -\frac{\omega_p^2}{\omega\omega_c} \ ; \quad \varepsilon_3 \simeq -\frac{\omega_p^2}{\omega^2} \ .$$

Note that in this frequency range, the ions only contribute to the quantity ε_1, through the term ω_{LH}^2, while the quantities ε_2 and ε_3 are determined solely by the electrons. Using general dispersion relation for electromagnetic waves in a cold magnetized plasma [see e.g. *Ginzburg and Rukhadze*, 1972], together with the expressions for the components of the dielectric tensor given above, one can derive the following dispersion relation in the frequency range of interest [*Shklyar and Jiříček*, 2000]

$$\omega^2 = \frac{\omega_{LH}^2}{1 + q^2/k^2} + \frac{\omega_c^2 \cos^2\theta}{(1 + q^2/k^2)^2} \equiv \omega_{LH}^2 \frac{k^2}{k^2 + q^2} + \omega_c^2 \frac{k_\|^2 k^2}{(k^2 + q^2)^2} \ , \tag{7}$$

where

$$q^2 = \frac{\omega_p^2}{c^2} \ , \tag{8}$$

and $k_\| = k\cos\theta$ and $k_\perp = k\sin\theta$. Figure 10 shows the so-called surface of the refractive index, i.e. the isolines of constant frequencies on the $(k_\perp, k_\|)$-plane, resulting from the dispersion relation (7). The contours shown correspond (from blue (inner) to brown (outer)) to the 14^{th}, 17^{th}, 20^{th}, 23^{rd}, 26^{th}, and 29^{th} harmonics of the proton cyclotron frequency. One can see that for any frequency, the largest possible value of $k_\|$ corresponds to parallel propagation, i.e., $k = k_\parallel$, $k_\perp = 0$; and since for $\omega \lesssim \omega_{LH}$, each term on the right hand side of (7) is smaller than ω_{LH}^2, so that the following inequalities should be fulfilled:

$$\frac{k_\parallel^2}{q^2} < \frac{\omega}{\omega_c} \lesssim \frac{\omega_{LH}}{\omega_c} \ll 1 \; ; \quad \frac{k^2}{q^2} < \frac{\omega^2}{\omega_{LH}^2 - \omega^2} \; . \tag{9}$$

Due to reasons clarified below, only waves propagating at a large angle θ to the ambient magnetic field will be considered.

In order to estimate typical values for the refractive index, the maximum parallel component of the wave vector, and the resonant velocity the following further assumptions are made. As can be seen from Figure 10, for $\omega \lesssim \omega_{LH}$, the wave refractive index N at large θ is of the same order as its value at $\theta = \pi/2$ (which is not true for $\omega = \omega_{LH}$). From (7) it then follows that in the case under discussion $k^2 \sim \omega_p^2/c^2$, or alternatively

$$N^2 \sim \frac{\omega_p^2}{\omega^2} \; . \tag{10}$$

Using the standard relations between the components of the polarization vector **a** [see e.g. *Shklyar and Matsumoto*, 2009]

$$a_y = -i\frac{\varepsilon_2}{N^2 - \varepsilon_1} a_x \; ; \quad a_z = \frac{N^2 \sin\theta \cos\theta}{N^2 \sin^2\theta - \varepsilon_3} a_x \; , \tag{11}$$

and the expressions for ε_1 , ε_2 , ε_3 given previously the polarisation vector can be rewritten as

$$a_y \sim i\frac{\omega}{\omega_c} a_x \ll a_x \; ; \quad a_z \sim \cos\theta \; a_x \ll a_x \; ,$$

so that the wave electric field is right-hand and almost linearly polarized along the x-axis.

As for the wave magnetic field, combining Faraday's law $[\mathbf{k} \times \mathbf{E}] = (\omega/\mathbf{c})\mathbf{B}$ and the relations given above it follows that

$$|B_x| \sim \frac{\omega_p}{\omega_c} \cos\theta \; a_x |E| \; ; |B_y| \sim \frac{\omega_p}{\omega} \cos\theta \; a_x |E| \; ; |B_z| \sim \frac{\omega_p}{\omega_c} \sin\theta \; a_x |E| \; ,$$

thus, $|B_x| \ll |B_y|$, $|B_z|$. It is worth mentioning that $|B| \gg |E|$ (in CGS units), but $|B| \ll N|E|$.

6.2. Propagation of magnetosonic waves in the magnetosphere

The surface of the refractive index, shown in Figure 10, provides information regarding the propagation on MSW. Since the wave group velocity is directed normal to the refractive index surface, for large θ except when considering propagation directions close to $\theta = \pi/2$, the wave group velocity is directed almost along the ambient magnetic field. In the vicinity of $\theta = \pi/2$, the direction of wave group velocity with respect to the ambient magnetic field changes sign very fast, so that the point where $\theta = \pi/2$ may be considered as a reflection point. Figure 11 shows an example of the ray trajectory of a 150 Hz magnetosonic wave propagating in meridian plane which starts at $L = 4.15$ on the equator and has a wave normal angle $\theta_0 = 89°$. We see that the latitude of the ray trajectory oscillates around zero, so that the trajectory as the whole is confined to the equatorial region. If the initial wave normal angle has an azimuthal component, the ray no longer lies in the meridian plane, but its confinement to the equatorial region remains in effect.

6.3. Magnetosonic wave excitation

Considering MSW excitation as the result of resonant interaction with energetic plasma particles, assuming cyclotron instability to be in effect the resonant velocity related to the nth cyclotron resonance is given by

$$V_{Rn\alpha} = \frac{\omega - n\omega_{H\alpha}}{k_{\parallel}} , \quad \alpha = e,\ i \tag{12}$$

where index α refers to quantities related to electrons (e) and protons (i), so that $\omega_{He} = \omega_c$ and $\omega_{Hi} = \Omega_p$. Equation (12) defines the particle parallel velocity at which it interacts resonantly with the wave. Since the waves are excited due to their interaction with resonant particles, and because the number of these particles depends on their energy and in particular their parallel velocity, the value of $V_{Rn\alpha}$ is essential for estimating the efficiency of their interaction. The value of $V_{Rn\alpha}$ may be estimated using the following parameters, which are typical of the equatorial region at $L = 4.15$, namely:

$$\omega \sim 900 \text{ rad/s} \; ; \;\; \omega_p \sim 6.4{\cdot}10^5 \text{ rad/s} \; ; \;\; \omega_c \sim 7.6{\cdot}10^4 \text{ rad/s} \; ; \;\; \Omega_c \sim 41.6 \text{ rad/s} \; ; \;\; \omega_{LH} \sim 1.8{\cdot}10^3 \text{ rad/s}$$

together with (see (10))

$$N \sim 677 \; ; \quad k \sim 2.1 \cdot 10^{-5}\text{cm}^{-1} \; . \tag{13}$$

The first inequality in (9) gives the maximum value of $k_{\|}$

$$(k_{\|})_{max} \sim 2.4 \cdot 10^{-6}\text{cm}^{-1} \; .$$

Obviously, this value corresponds to the parallel propagation of MSW. Using this value we find that, in general

$$|V_{R1e}| > 3.2 \cdot 10^{10}\text{cm/s} \; ; \; V_{R1i} > 3.8 \cdot 10^{8}\text{cm/s} \; ; \; V_{R0} > 4 \cdot 10^{8}\text{cm/s} \; .$$

Note that the Cerenkov resonance velocity (V_{R0}) does not depend on the type of particle, in contrast to cyclotron resonance velocities.

Relation (12) is written using the non-relativistic approximation. In this approximation, it may be seen that the interaction of MSW with electrons at the first cyclotron resonance - the only one that exists for parallel propagation - is impossible. As for the protons, the value of $V_{\|} = V_{R1i}$ corresponds to proton energies exceeding 100 keV, and so only a small number of resonant particles may be expected in this case. Thus, it is necessary to consider oblique MSW propagation. In this case the Cerenkov resonance comes into effect, playing the main role together with the first cyclotron resonance, for small and medium wave normal angles. For oblique propagation, the value of V_{R0} given above represents the minimum value of parallel velocity, corresponding to $E > 65$ eV electrons and $E > 118$ keV ions. In the absence of parallel beams, the Cerenkov resonance leads to wave damping and, given the relation between resonance energies, drives out a possible wave excitation at the first cyclotron resonance due to cyclotron instability. Thus, the only possible case for MSW excitation is when $k_\| \ll (k_\|)_{max}$, i.e., when the wave normal angle is close to $\pi/2$ and $\omega \simeq n\Omega_c$. In this case, the Cerenkov resonance for electrons does not drive out the instability, since it corresponds to an overly high electron velocity, while V_{Rni} for protons can be sufficiently small for an appropriate number of particles to be in cyclotron resonance. As was shown by *Shklyar* [1986], higher order cyclotron resonances for protons are efficient only when

$$k_\| V_\| + k_\perp V_\perp > \omega \ ,$$

which requires $V_\perp > \omega/k$. Using (13) it is found that $V_\perp > 4.5 \cdot 10^7$cm/s, or $E > 1$ keV, which is quite realistic for protons.

A general expression for the growth rate of the cyclotron instability for oblique electromagnetic wave, which is valid for MSW under consideration, can be found in *Shklyar and Matsumoto* [2009, expression (4.13)]. As has been argued above, the growth rate is significant only for $\omega \simeq n\Omega_c$, with the main contribution to the growth rate from protons interacting with the wave at the nth cyclotron resonance. Retaining the corresponding term for the growth rate from *Shklyar and Matsumoto* [2009] it is found that

$$\gamma = \frac{\Omega_c(\pi e|E|c)^2}{2m_i k_\| U} \int_0^\infty d\mu f'_{0n}(\mu) V_n^2(\mu) \ , \tag{14}$$

where f_0 is the unperturbed proton distribution function, which depends on particle energy W and magnetic momentum μ,

$$f'_{0n} = \left(\frac{\partial f_0}{\partial W} + \frac{n}{\omega} \frac{\partial f_0}{\partial \mu} \right)_{W = m_i V_{Rni}^2/2 + \mu \Omega_c} , \tag{15}$$

$$V_n = \left(\frac{n|\Omega_c|}{k_\perp c} a_x + \frac{V_{Rni}}{c} a_z \right) J_n(\rho) + \frac{i\rho\Omega_c}{k_\perp c} a_y J'_n(\rho) \; ; \quad \rho = k_\perp \left(\frac{2\mu}{m_i |\Omega_c|} \right)^{1/2} , \tag{16}$$

and $J_n(\rho)$ and $J'_n(\rho)$ are, respectively, the Bessel function and its derivative with respect to the argument ρ. The quantity ρ defined above is the dimensionless Larmor radius, i.e., $\rho = k_\perp V_\perp / \Omega_c$. The quantity U that enters the expression for γ is the wave energy density and is proportional to $|E|^2$ and expressed through the polarization coefficients and the dielectric tensor in a usual way [e.g. *Shafranov*, 1967]. The value of V_n, which plays the role of an effective amplitude of interaction at the nth cyclotron resonance is proportional to $J_n(\rho)$. It is well known that for large n this function is exponentially small unless $\rho \equiv k_\perp V_\perp / \Omega_c > n$, or, with the account of $n \simeq \omega/\Omega_c$, $k_\perp V_\perp > \omega$. This explains the above mentioned requirement of the efficiency of wave excitation by ions.

From (14)-(16) it follows that for wave excitation the derivative (15) should, on average, be positive, which is typically observed for distributions with a loss-cone or temperature anisotropy. In general, the growth rate strongly depends on the energetic proton distribution function, as well as on the wave characteristics (frequency and wave vector). However, in many cases the distribution function is proportional to $\exp(-W/W_T)$, where W_T is a characteristic energy scale of the distribution. (For a quasi-Maxwellian distribution, W_T characterizes the particle thermal energy). In this case, the growth rate γ defined by (14) appears to be proportional to

$$\exp \left(- \frac{m_i (\omega - n\Omega_c)^2}{2 k_\parallel^2 W_T} \right)$$

As mentioned above, $k_{\parallel}$ is a small quantity, which clearly shows that the growth rate is significant only for $\omega \simeq n\Omega_c$, i.e., for frequencies close to ion cyclotron harmonics.

6.4. Comparison of Experimental and Theoretical Dispersion

The dispersion relation (7) is plotted as the solid line in Figure 12 using plasma densities of 19 cm^{-3} (black) and 15 cm^{-3} estimated using data from WHISPER. The angle between the wave propagation vector and the eternal magnetic field was assumed to be 89°. In order to fit the experimentally derived dispersion to the theoretical ones n, the ambiguity factor in equation (2) was varied in the range $-5 < n < 5$ and the results compared to the theoretical curves. It was found that the best fit was obtained using $n = 1$ and the dispersions of the Bx (blue crosses) and Bz (cyan circles) components using this factor are shown in the Figure. This value is in agreement with the fact that the wavelength of the magnetosonic waves is ∼18 km (from the dispersion shown in Figure 12) compared with an intersatellite separation of 60 km. As can be seen from this Figure there is good agreement between the experimental and theoretical results.

7. Conclusions

Using data collected as part of the Cluster Inner Magnetosphere campaign this paper has presented observations of a set of narrow banded emissions that occurred in the vicinity of harmonics of the proton gyrofrequency. It was demonstrated that these waves propagated in the magnetosonic mode as characterised by their spectral properties.

Using the phase differencing method, it was possible to combine observations from the satellites Cluster 3 and Cluster 4 in order to determine the dispersion relation. The experimentally determined dispersion was shown to be consistent with theoretical dispersion curves.

Acknowledgments. SNW and MAB wish to acknowledge financial support from International Space Science Institute, Bern, Royal Society Collaboration grant, UK EPSRC grant EP/H00453X/1, and the European Union's Horizon 2020 research and innovation programme under grant agreement No 637302. The authors would like to thank the Cluster instrument teams for provision of the data used in this paper. These data are available from the Cluster Science Archive (http://www.cosmos.esa.int/web/csa).

References

Albert, J. M. (2008), Efficient approximations of quasi-linear diffusion coefficients in the radiation belts, *J. Geophys. Res. (Space Physics)*, *113*, A06208, doi: 10.1029/2007JA012936.

André, R., F. Lefeuvre, F. Simonet, and U. S. Inan (2002), A first approach to model the low-frequency wave activity in the plasmasphere, *Annales Geophysicae*, *20*, 981–996, doi:10.5194/angeo-20-981-2002.

Balikhin, M., S. Walker, R. Treumann, H. Alleyne, V. Krasnoselskikh, M. Gedalin, M. Andre, M. Dunlop, and A. Fazakerley (2005), Ion sound wave packets at the quasiperpendicular shock front, *Geophys. Res. Lett.*, *32*(24), L24,106, doi:10.1029/2005GL024660.

Balikhin, M. A., and M. E. Gedalin (1993), Comparative analysis of different methods for distinguishing temporal and spatial variations, in *Proc. of START Conf., Aussois, France*, vol. ESA WPP 047, pp. 183–187.

Balikhin, M. A., L. J. C. Woolliscroft, H. S. Alleyne, M. Dunlop, and M. A. Gedalin

(1997a), Determination of the dispersion of low frequency waves downstream of a quasi-perpendicular collisionless shock, *Annales Geophysicae*, *15*(2), 143–151.

Balikhin, M. A., T. Dudok de Witt, L. J. C. Woolliscroft, S. N. Walker, H. Alleyne, V. Krasnoselskikh, W. A. C. Mier–Jedrzejowicz, and W. Baumjohann (1997b), Experimental determination of the dispersion of waves observed upstream of a quasi–perpendicular shock, *Geophys. Res. Lett.*, *24*, 787–790, doi:10.1029/97GL00671.

Balikhin, M. A., S. N. Walker, T. Dudok de Witt, H. S. Alleyne, L. J. C. Woolliscroft, W. A. C. Mier-Jedrzejowicz, and W. Baumjohann (1997c), Nonstationarity and low frequency turbulence at a quasi-perpendicular shock front, *Adv. Sp. Res.*, *20*(4-5), 729–734, doi:10.1016/S0273-1177(97)00463-8.

Balikhin, M. A., S. Schwartz, S. N. Walker, H. S. C. K. Alleyne, M. Dunlop, and H. Lühr (2001), Dual-spacecraft observations of standing waves in the magnetosheath, *J. Geophys. Res.*, *106*(A11), 25,395–25,408, doi:10.1029/2000JA900096.

Balikhin, M. A., O. A. Pokhotelov, S. N. Walker, E. Amata, M. Andre, M. Dunlop, and H. S. K. Alleyne (2003), Minimum variance free wave identification: Application to Cluster electric field data in the magnetosheath, *Geophys. Res. Lett.*, *30*(10), 15-1, doi:10.1029/2003GL016918.

Balikhin, M. A., Y. Y. Shprits, S. N. Walker, L. Chen, N. Cornilleau-Wehrlin, I. Dandouras, O. Santolik, C. Carr, K. H. Yearby, and B. Weiss (2015), Observations of discrete harmonics emerging from equatorial noise, *Nat Commun*, *6*, doi:10.1038/ncomms8703.

Balogh, A., M. W. Dunlop, S. W. H. Cowley, D. J. Southwood, J. G. Thomlinson, K. H. Glassmeier, G. Musmann, H. Lühr, S. Buchert, M. H. Acuña, D. H. Fairfield, J. A.

Slavin, W. Riedler, K. Schwingenschuh, and M. G. Kivelson (1997), The Cluster magnetic field investigation, *Sp. Sci. Rev.*, *79*, 65–91, doi:10.1023/A:1004970907748.

Boardsen, S. A., D. L. Gallagher, D. A. Gurnett, W. K. Peterson, and J. L. Green (1992), Funnel-shaped, low-frequency equatorial waves, *J. Geophys. Res.*, *97*, 14,967, doi:10.1029/92JA00827.

Boardsen, S. A., G. B. Hospodarsky, C. A. Kletzing, R. F. Pfaff, W. S. Kurth, J. R. Wygant, and E. A. MacDonald (2014), Van Allen Probe observations of periodic rising frequencies of the fast magnetosonic mode, *Geophys. Res. Lett.*, *41*, 8161–8168, doi: 10.1002/2014GL062020.

Bortnik, J., and R. M. Thorne (2010), Transit time scattering of energetic electrons due to equatorially confined magnetosonic waves, *J. Geophys. Res. (Space Physics)*, *115*, A07213, doi:10.1029/2010JA015283.

Chen, L., and R. M. Thorne (2012), Perpendicular propagation of magnetosonic waves, *Geophys. Res. Lett.*, *39*, L14102, doi:10.1029/2012GL052485.

Chen, L., R. M. Thorne, V. K. Jordanova, and R. B. Horne (2010), Global simulation of magnetosonic wave instability in the storm time magnetosphere, *J. Geophys. Res. (Space Physics)*, *115*(A11), A11222, doi:10.1029/2010JA015707.

Chen, L., R. M. Thorne, V. K. Jordanova, M. F. Thomsen, and R. B. Horne (2011), Magnetosonic wave instability analysis for proton ring distributions observed by the lanl magnetospheric plasma analyzer, *J. Geophys. Res. (Space Physics)*, *116*, A03223, doi:10.1029/2010JA016068.

Chisham, G., S. J. Schwartz, M. Balikhin, and M. W. Dunlop (1999), AMPTE observations of mirror mode waves in the magnetosheath: Wavevector determination, *J.*

Geophys. Res. A, *104*(A1), 437–447, doi:10.1029/1998JA900044.

Cornilleau-Wehrlin, N., P. Chauveau, S. Louis, A. Meyer, J. M. Nappa, S. Perraut, L. Rezeau, P. Robert, A. Roux, C. De Villedary, Y. de Conchy, L. Friel, C. C. Harvey, D. Hubert, C. Lacombe, R. Manning, F. Wouters, F. Lefeuvre, M. Parrot, J. L. Pinçon, B. Poirier, W. Kofman, P. Louarn, and the STAFF Investigator Team (1997), The Cluster Spatio-Temporal Analysis of Field Fluctuations (STAFF) experiment, *Sp. Sci. Rev.*, *79*, 107–136.

Dawson, J. (1961), On landau damping, *Phys. Fluids*, *4*, 869–874, doi:10.1063/1.1706419.

Décréau, P. M. E., P. Fergeau, V. Krannosels'kikh, M. Leveque, P. Martin, O. Randriamboarison, F. X. Sene, J. G. Trotignon, P. Canu, and P. B. Mogensen (1997), WHISPER, a resonance sounder and wave analyser: Performances and perspectives for the Cluster mission, *Sp. Sci. Rev.*, *79*, 157–193, doi:10.1023/A:1004931326404.

Fu, H. S., J. B. Cao, Z. Zhima, Y. V. Khotyaintsev, V. Angelopoulos, O. Santolik, Y. Omura, U. Taubenschuss, L. Chen, and S. Y. Huang (2014), First observation of rising-tone magnetosonic waves, *Geophys. Res. Lett.*, *41*(21), 7419–7426, doi:10.1002/2014GL061687.

Ginzburg, V. L., and A. A. Rukhadze (1972), Waves in magnetoactive plasma, in *Handbook of Physics*, vol. 49, edited by S. Flügge, p. 395, Springer, Berlin.

Gurnett, D. A. (1976), Plasma wave interactions with energetic ions near the magnetic equator, *J. Geophys. Res.*, *81*, 2765–2770, doi:10.1029/JA081i016p02765.

Gurnett, D. A., R. L. Huff, and D. L. Kirchner (1997), The wide-band plasma wave investigation, *Sp. Sci. Rev.*, *79*, 195–208.

Gustafsson, G., R. Boström, B. Holback, G. Holmgren, A. Lundgren, K. Stasiewicz, L. Åéhlen, F. S. Mozer, D. Pankow, P. Harvey, P. Berg, R. Ulrich, A. Pedersen, R. Schmidt, A. Butler, A. W. C. Fransen, D. Klinge, M. Thomsen, C.-G. Falthammar, P.-A. Lindqvist, S. Christenson, J. Holtet, B. Lybekk, T. A. Sten, P. Tanskanen, K. Lappalainen, and J. Wygant (1997), The Electric Field and Wave experiment for the Cluster mission, *Sp. Sci. Rev.*, *79*, 137–156.

Horne, R. B., G. V. Wheeler, and H. S. C. K. Alleyne (2000), Proton and electron heating by radially propagating fast magnetosonic waves, *J. Geophys. Res.*, *105*, 27,597–27,610, doi:10.1029/2000JA000018.

Horne, R. B., R. M. Thorne, S. A. Glauert, N. P. Meredith, D. Pokhotelov, and O. Santolík (2007), Electron acceleration in the Van Allen radiation belts by fast magnetosonic waves, *Geophys. Res. Lett.*, *34*, L17,107, doi:10.1029/2007GL030267.

Kasahara, Y., H. Kenmochi, and I. Kimura (1994), Propagation characteristics of the elf emissions observed by the satellite akebono in the magnetic equatorial region, *Radio Sci.*, *29*, 751–767, doi:10.1029/94RS00445.

Korth, A., G. Kremser, A. Roux, S. Perraut, J.-A. Sauvaud, J.-M. Bosqued, A. Pedersen, and B. Aparicio (1983), Drift boundaries and ulf wave generation near noon at geostationary orbit, *Geophys. Res. Lett.*, *10*, 639–642, doi:10.1029/GL010i008p00639.

Korth, A., G. Kremser, S. Perraut, and A. Roux (1984), Interaction of particles with ion cyclotron waves and magnetosonic waves. observations from GEOS 1 and GEOS 2., *Planet. Sp. Sci.*, *32*(11), 1393–1406.

Laakso, H., H. Junginger, R. Schmidt, A. Roux, and C. de Villedary (1990), Magnetosonic waves above fc(H^+) at geostationary orbit - GOES 2 results, *J. Geophys. Res.*, *95*, 10,609–10,621, doi:10.1029/JA095iA07p10609.

Ma, Q., W. Li, L. Chen, R. M. Thorne, and V. Angelopoulos (2014), Magnetosonic wave excitation by ion ring distributions in the earth's inner magnetosphere, *J. Geophys. Res. (Space Physics)*, *119*, 844–852, doi:10.1002/2013JA019591.

Meredith, N. P., R. B. Horne, and R. R. Anderson (2008), Survey of magnetosonic waves and proton ring distributions in the earth's inner magnetosphere, *J. Geophys. Res. (Space Physics)*, *113*(A6), A06213, doi:10.1029/2007JA012975.

Mourenas, D., A. V. Artemyev, O. V. Agapitov, and V. Krasnoselskikh (2013), Analytical estimates of electron quasi-linear diffusion by fast magnetosonic waves, *J. Geophys. Res. (Space Physics)*, *118*, 3096–3112, doi:10.1002/jgra.50349.

Němec, F., O. Santolík, K. Gereová, E. Macúšová, Y. de Conchy, and N. Cornilleau-Wehrlin (2005), Initial results of a survey of equatorial noise emissions observed by the Cluster spacecraft, *Planet. Sp. Sci.*, *53*, 291–298, doi:10.1016/j.pss.2004.09.055.

Němec, F., O. Santolík, Z. Hrbáčková, J. S. Pickett, and N. Cornilleau-Wehrlin (2015), Equatorial noise emissions with quasiperiodic modulation of wave intensity, *J. Geophys. Res. (Space Physics)*, *120*, 2649–2661, doi:10.1002/2014JA020816.

O'Neil, T. (1965), Collisionless damping of nonlinear plasma oscillations, *Phys. Fluids*, *8*, 2255–2262, doi:10.1063/1.1761193.

Pedersen, A., N. Cornilleau-Wehrlin, B. De La Porte, A. Roux, A. Bouabdellah, P. M. E. Décréau, F. Lefeuvre, F. X. Séne, D. Gurnett, R. Huff, G. Gustafsson, G. Holmgren, L. Woolliscroft, H. S. Alleyne, J. A. Thompson, and P. H. N. Davies (1997), The Wave Experiment Consortium (WEC), *Sp. Sci. Rev.*, *79*, 93–106.

Perraut, S., A. Roux, P. Robert, R. Gendrin, J. A. Sauvaud, J. M. Bosqued, G. Kremser, and A. Korth (1982), A systematic study of ulf waves above f_{H+} from geos 1 and 2 measurements and their relationship with proton ring distributions, *J. Geophys. Res. A*, *87*, 6219.

Pinçon, J.-L., and F. Lefeuvre (1992), The application of the generalized Capon method to the analysis of a turbulent field in space plasma: Experimental constraints, *J. Atmos. Terr. Phys.*, *54*, 1237–1247.

Reme, H., J. M. Bosqued, J. A. Sauvaud, A. Cros, J. Dandouras, C. Aoustin, J. Bouyssou, T. Camus, J. Cuvilo, C. Martz, J. L. Médale, H. Perrier, D. Romefort, J. Rouzaud, D. D'Uston, E. Möbius, K. Crocker, M. Granoff, L. M. Kistler, M. Popecki, D. Hovestadt, B. Klecker, G. Paschmann, M. Scholer, C. W. Carlson, D. W. Curtis, R. P. Lin, J. P. McFadden, V. Formisano, E. Amata, M. B. Bavassano-Cattaneo, P. Baldetti, G. Belluci, R. Bruno, G. Chionchio, A. di Lellis, E. G. Shelley, A. G. Ghielmetti, W. Lennartsson, A. Korth, U. Rosenbauer, R. Lundin, S. Olsen, G. K. Parks, M. McCarthy, and H. Balsiger (1997), The Cluster ion spectrometry (cis) experiment, *Sp. Sci. Rev.*, *79*, 303–350, doi:10.1023/A:1004929816409.

Roberts, C. S., and M. Schulz (1968), Bounce resonant scattering of particles trapped in the Earth's magnetic field, *J. Geophys. Res.*, *73*(23), 7361–7376.

Russell, C. T., R. E. Holzer, and E. J. Smith (1970), OGO 3 observations of ELF noise in the magnetosphere: 2. the nature of the equatorial noise, *J. Geophys. Res.*, *75*, 755, doi:10.1029/JA075i004p00755.

Santolík, O., J. S. Pickett, D. A. Gurnett, M. Maksimovic, and N. Cornilleau-Wehrlin (2002), Spatiotemporal variability and propagation of equatorial noise observed by Cluster, *J. Geophys. Res. A*, *107*(A12), 43–1, doi:10.1029/2001JA009159.

Santolik, O., M. Parrot, and F. Lefeuvre (2003), Singular value decomposition methods for wave propagation analysis, *Radio Sci.*, *38*(1), 10–1, doi:10.1029/2000RS002523.

Shafranov, V. D. (1967), Electromagnetic waves in a plasma, *Reviews of Plasma Physics*, *3*, 1.

Shklyar, D., and H. Matsumoto (2009), Oblique whistler-mode waves in the inhomogeneous magnetospheric plasma: Resonant interactions with energetic charged particles, *Surveys in Geophysics*, *30*, 55–104, doi:10.1007/s10712-009-9061-7.

Shklyar, D. R. (1986), Particle interaction with an electrostatic vlf wave in the magnetosphere with an application to proton precipitation, *Planet. Sp. Sci.*, *62*, 347–370.

Shklyar, D. R., and F. Jiříček (2000), Simulation of nonducted whistler spectrograms observed aboard the magion 4 and 5 satellites, *J. Atmos. Sol. Terr. Phys.*, *62*, 347–370, doi:10.1016/S1364-6826(99)00097-8.

Shprits, Y. Y. (2009), Potential waves for pitch-angle scattering of near-equatorially mirroring energetic electrons due to the violation of the second adiabatic invariant, *Geophys. Res. Lett.*, *36*, L12106, doi:10.1029/2009GL038322.

Shprits, Y. Y., S. R. Elkington, N. P. Meredith, and D. A. Subbotin (2008), Review of modeling of losses and sources of relativistic electrons in the outer radiation belt i: Radial transport, *J. Atmos. Sol. Terr. Phys.*, *70*, 1679–1693, doi:10.1016/j.jastp.2008.06.008.

Shprits, Y. Y., D. Subbotin, and B. Ni (2009), Evolution of electron fluxes in the outer radiation belt computed with the verb code, *J. Geophys. Res. (Space Physics)*, *114*(A13), A11209, doi:10.1029/2008JA013784.

Thomsen, M. F., M. H. Denton, V. K. Jordanova, L. Chen, and R. M. Thorne (2011), Free energy to drive equatorial magnetosonic wave instability at geosynchronous orbit, *J. Geophys. Res. (Space Physics)*, *116*, A08220, doi:10.1029/2011JA016644.

Tsyganenko, N. A. (1989), A magnetospheric magnetic field model with a warped tail current sheet, *Planet. Sp. Sci.*, *37*, 5–20, doi:10.1016/0032-0633(89)90066-4.

Walker, S. N., and I. Moiseenko (2013), Determination of wave vectors using the phase differencing method, *Annales Geophysicae*, *31*(9), 1611–1617, doi:10.5194/angeo-31-1611-2013.

Walker, S. N., F. Sahraoui, M. A. Balikhin, G. Belmont, J.-L. Pinçon, L. Rezeau, H. Alleyne, N. Cornilleau-Wehrlin, and M. André (2004), A comparison of wave mode identification techniques, *Annales Geophysicae*, *22*(8), 3021–3032.

Woolliscroft, L. J. C., H. S. C. Alleyne, C. M. Dunford, A. Sumner, J. A. Thompson, S. N. Walker, K. H. Yearby, A. Buckley, S. Chapman, and M. P. Gough (1997), The Digital Wave Processing Experiment on Cluster, *Sp. Sci. Rev.*, *79*, 209–231, doi:10.1023/A:1004914211866.

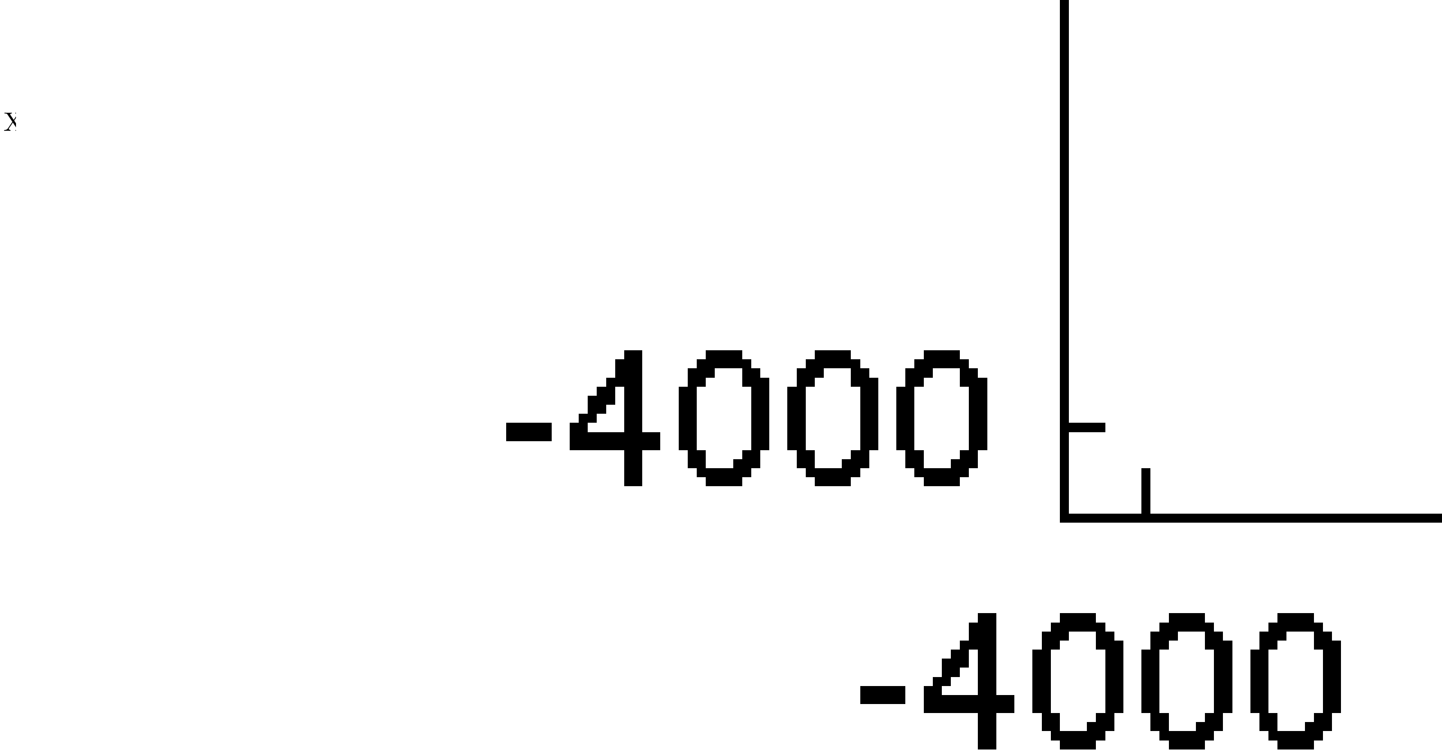

Figure 1. Location of the Cluster spacecraft on July 6^{th}, 2013 (lower right panel) and their relative separations (C1 black, C2 red, C3 green, and C4 blue). Note that due to their close proximity C3 is masked by C4 and their trajectories in the lower right panel appear magenta.

Figure 2. Dynamic spectra of the SM B_z component of the STAFF magnetic field waveform measured onboard spacecraft 3 (panel a) and 4 (panel b) on July 6^{th}, 2013. The black curves represent the 15, 20, 25, and 30^{th} harmonics of the proton gyrofrequency Ω_p.

Figure 3. FFT spectra of the Bx component of the STAFF magnetic field waveform measured onboard spacecraft 4 on July 6^{th}, 2013. The black curves represent harmonics of the proton gyrofrequency in the range 14-30 Ω_p.

Figure 4. FFT spectrum of the Bx component of the STAFF magnetic field waveform measured onboard spacecraft 4 during the period 18:48:40-18:49:20 UT. The vertical lines represent harmonics of the proton gyrofrequency, each labelled with the harmonic number.

Figure 5. Spectra of the ion distribution measured by CIS-CODIF on July 6^{th}, 2013 between 1840 and 1857UT.

Figure 6. Frequency of peak growth rate with respect to the Alfvén and ring velocities.

Figure 7. The characteristic properties of the banded emissions. From top to bottom the panels show the wave spectra, the ellipticity of the waves, the angle between the propagation direction and the external magnetic field, and the angle between the maximum variance direction and the external magnetic field.

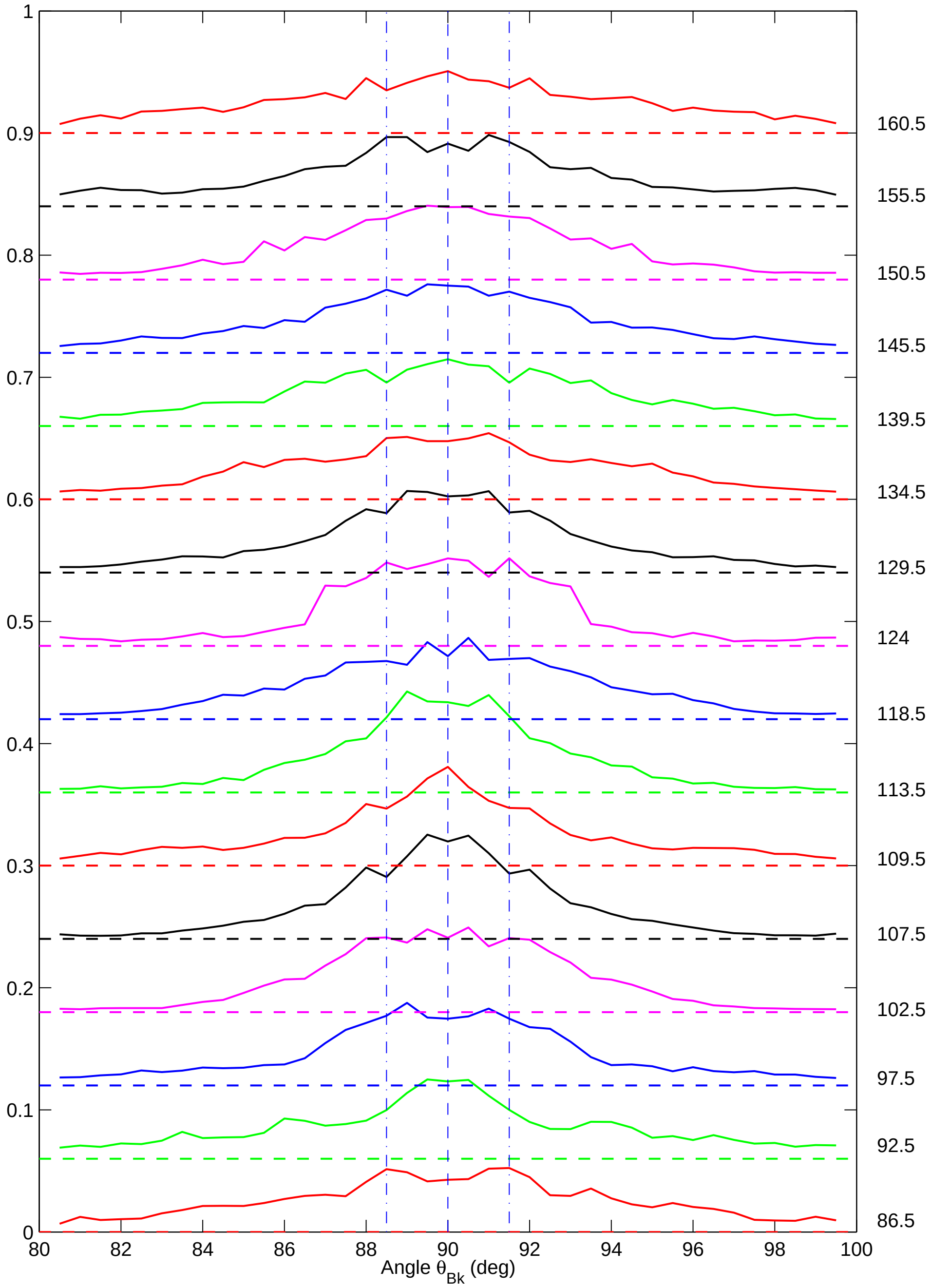

Figure 8. Distributions of the wave normal angle for frequencies at which the banded harmonic emissions occurred.

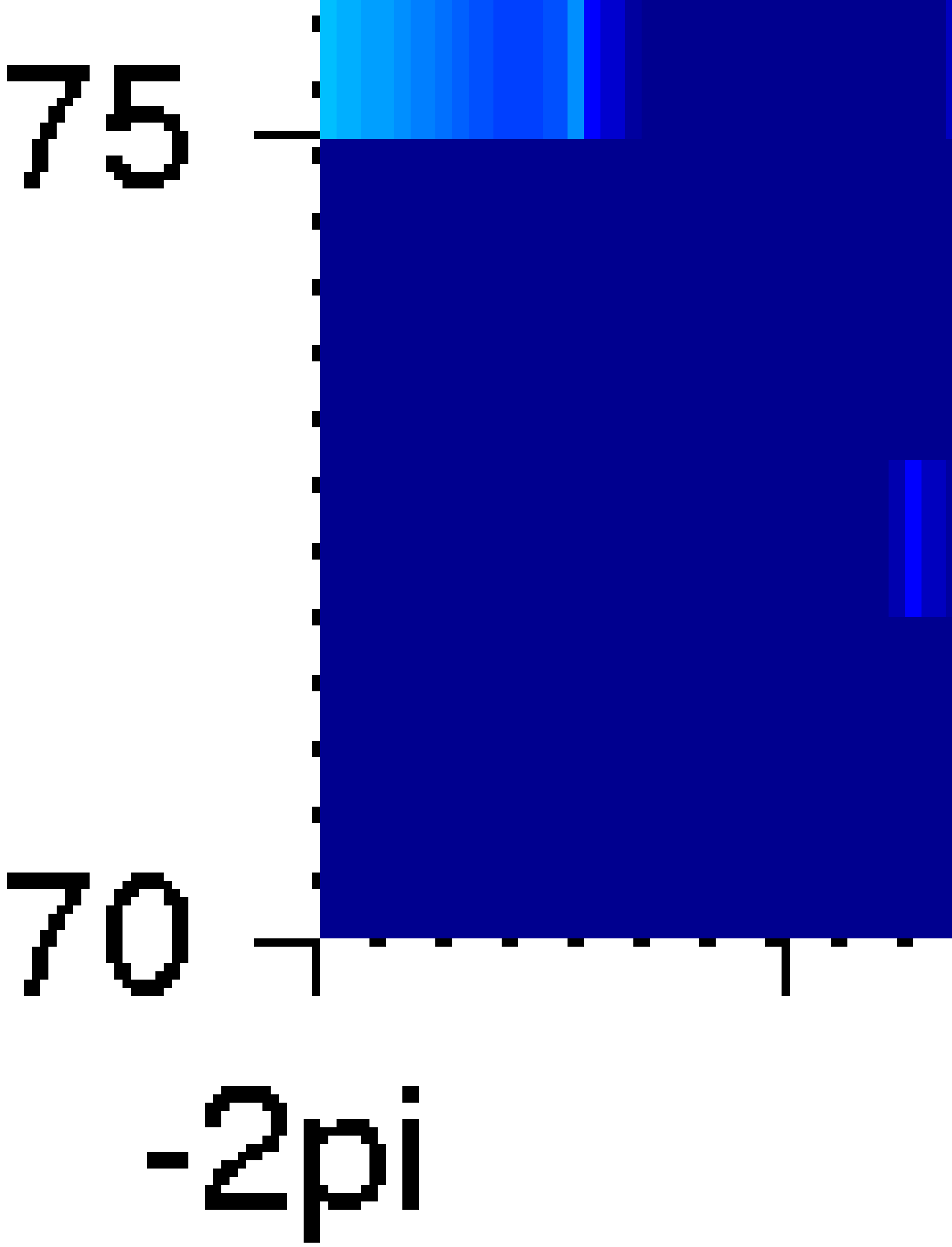

Figure 9. $\omega - k$ histogram showing the variation in the phase difference of the signals measured be satellites C3 and C4 with frequency.

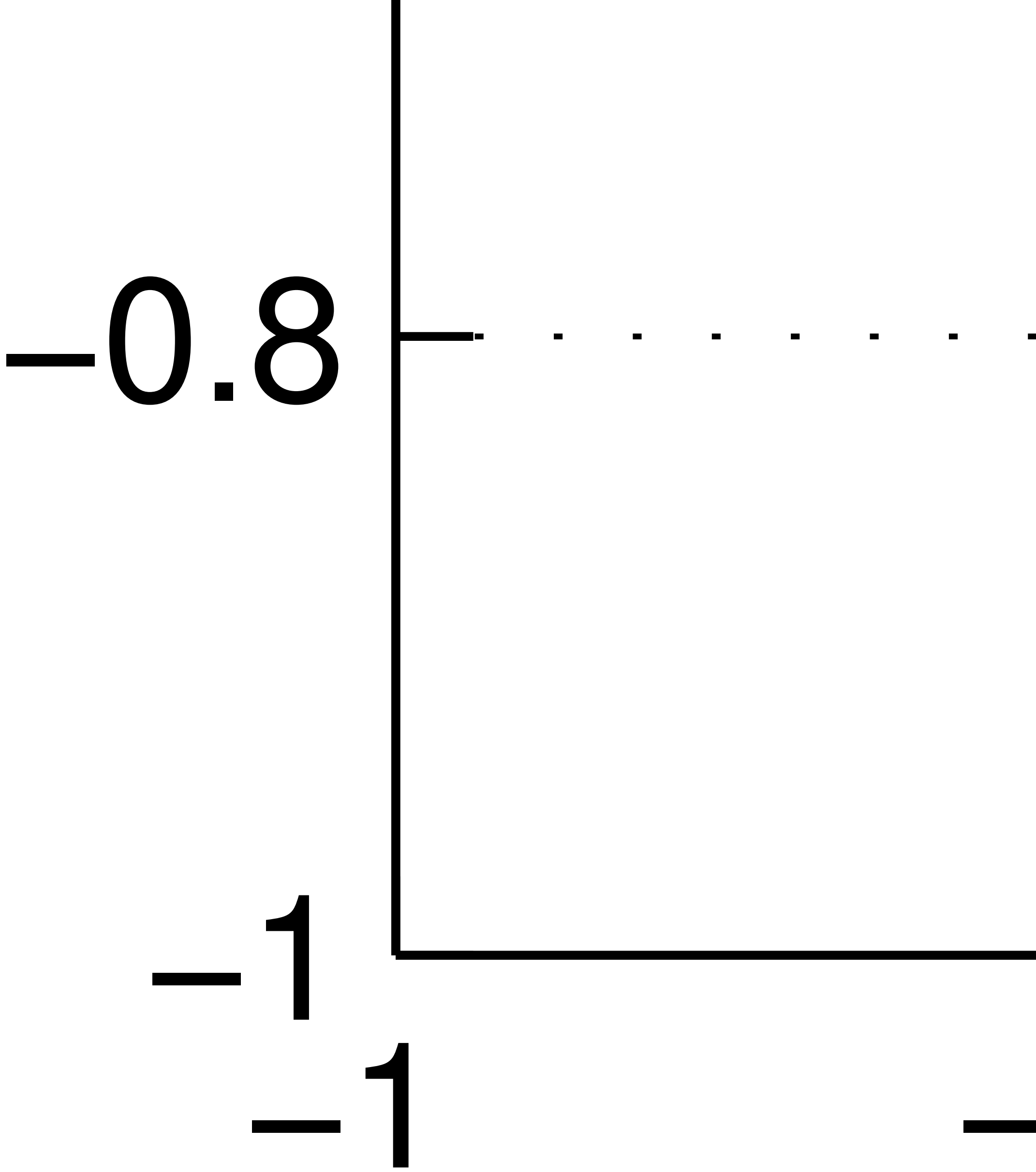

Figure 10. The surface of refractive index for the dispersion relation (7).

Figure 11. The trajectory oscillates around the equator with the deviation $\lesssim 5°$.

Figure 12. Comparison of the experimentally determined dispersion using the Bz (blue lines and crosses) and Bx (cyan lines and circles) components with that derived theoretically from Eqn 7 using total plasma densities of 19 cm^{-3} (black) and 15 cm^{-3} (red). θ_{kB} was assumed to be 89°.

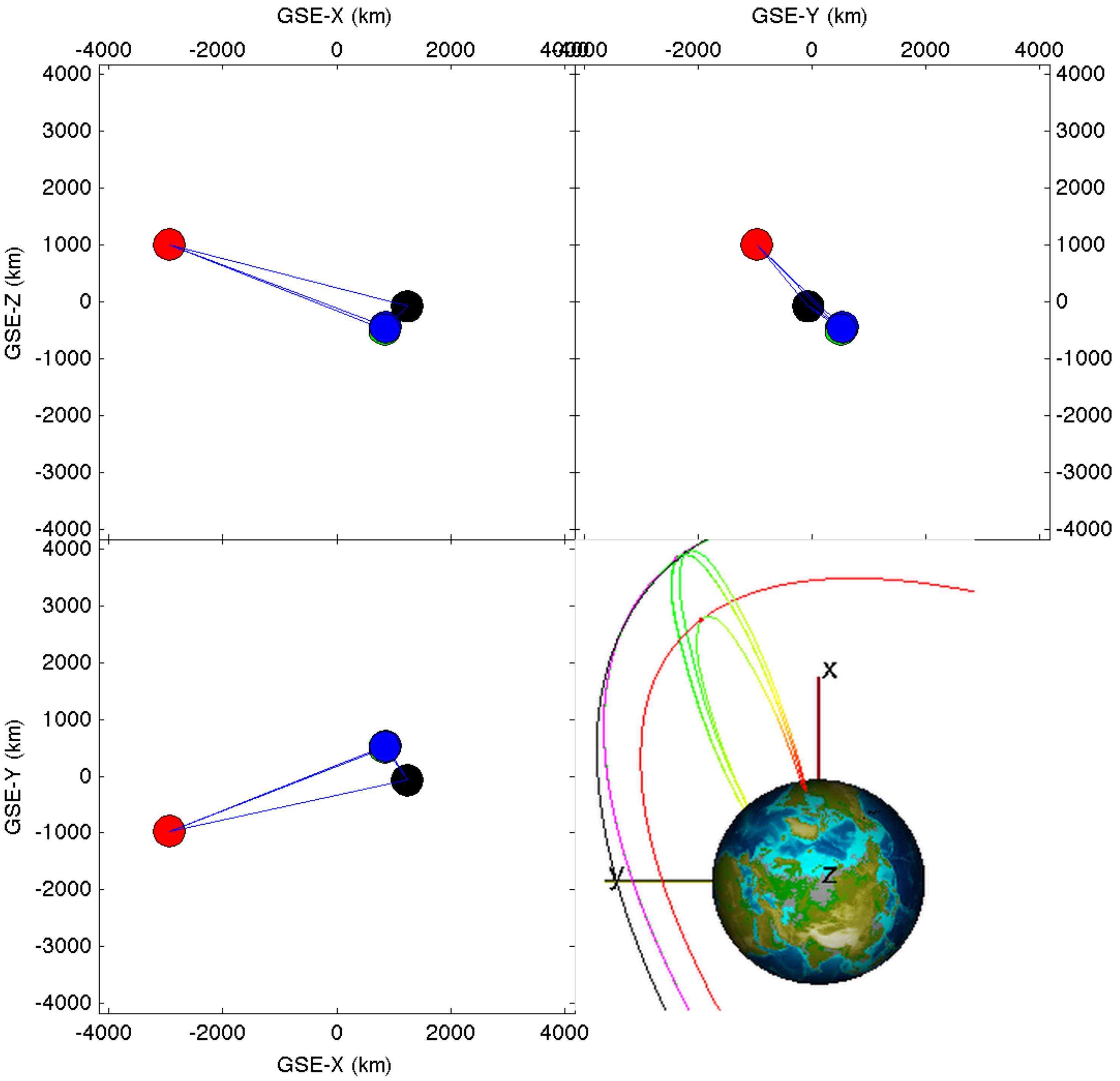
GSE-X (km)
GSE-Y (km)
GSE-Z (km)
GSE-Y (km)
GSE-X (km)
-4000
-2000
0
2000
4000
-1000
-3000
1000
3000
X
Y
Z

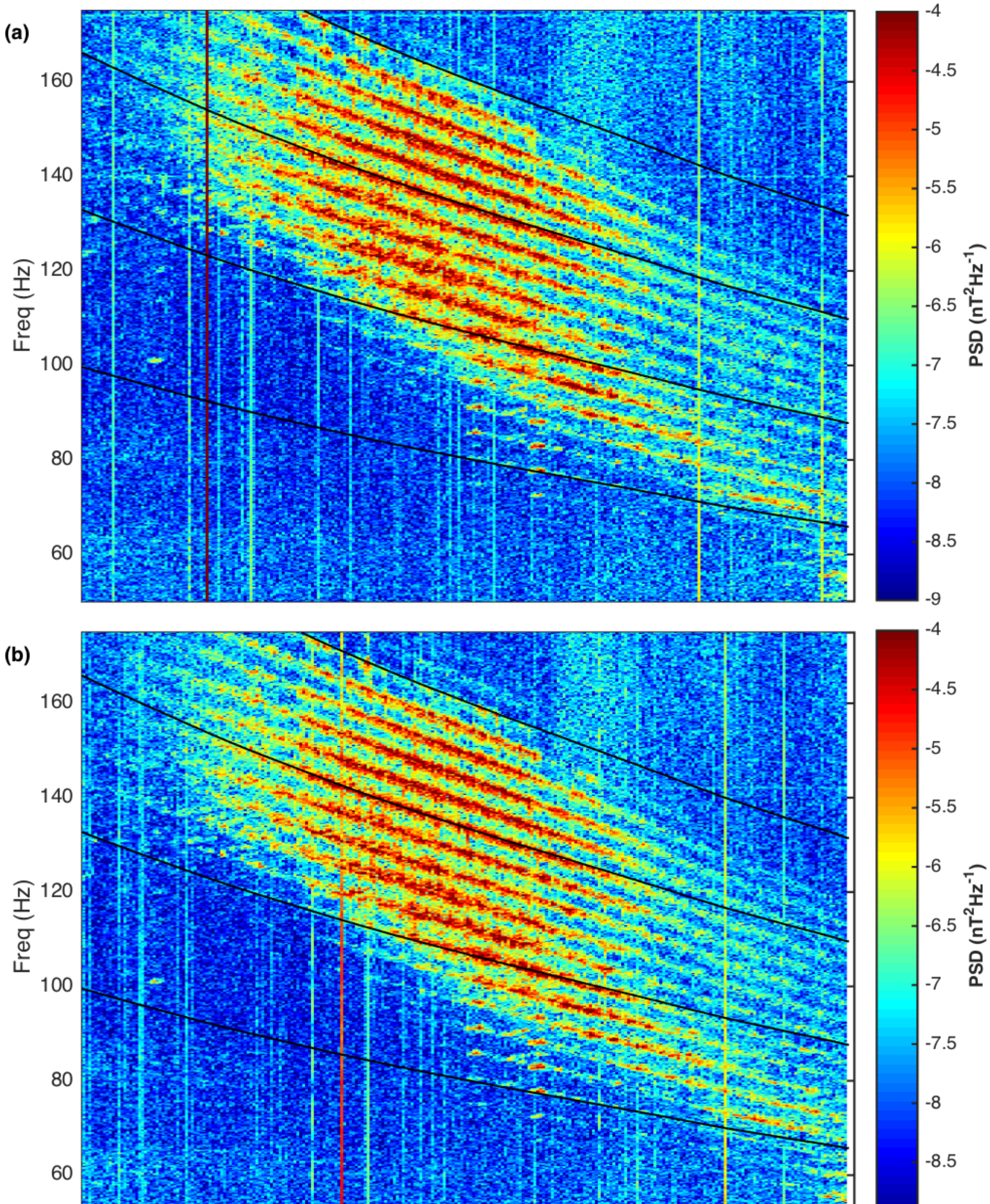

(a)
(b)
Freq (Hz)
160
140
120
100
80
60
PSD (nT^{2}Hz^{-1})
-4
-4.5
-5
-5.5
-6
-6.5
-7
-7.5
-8
-8.5
-9
18:40:00
18:45:00
18:50:00
18:55:00
Time UT

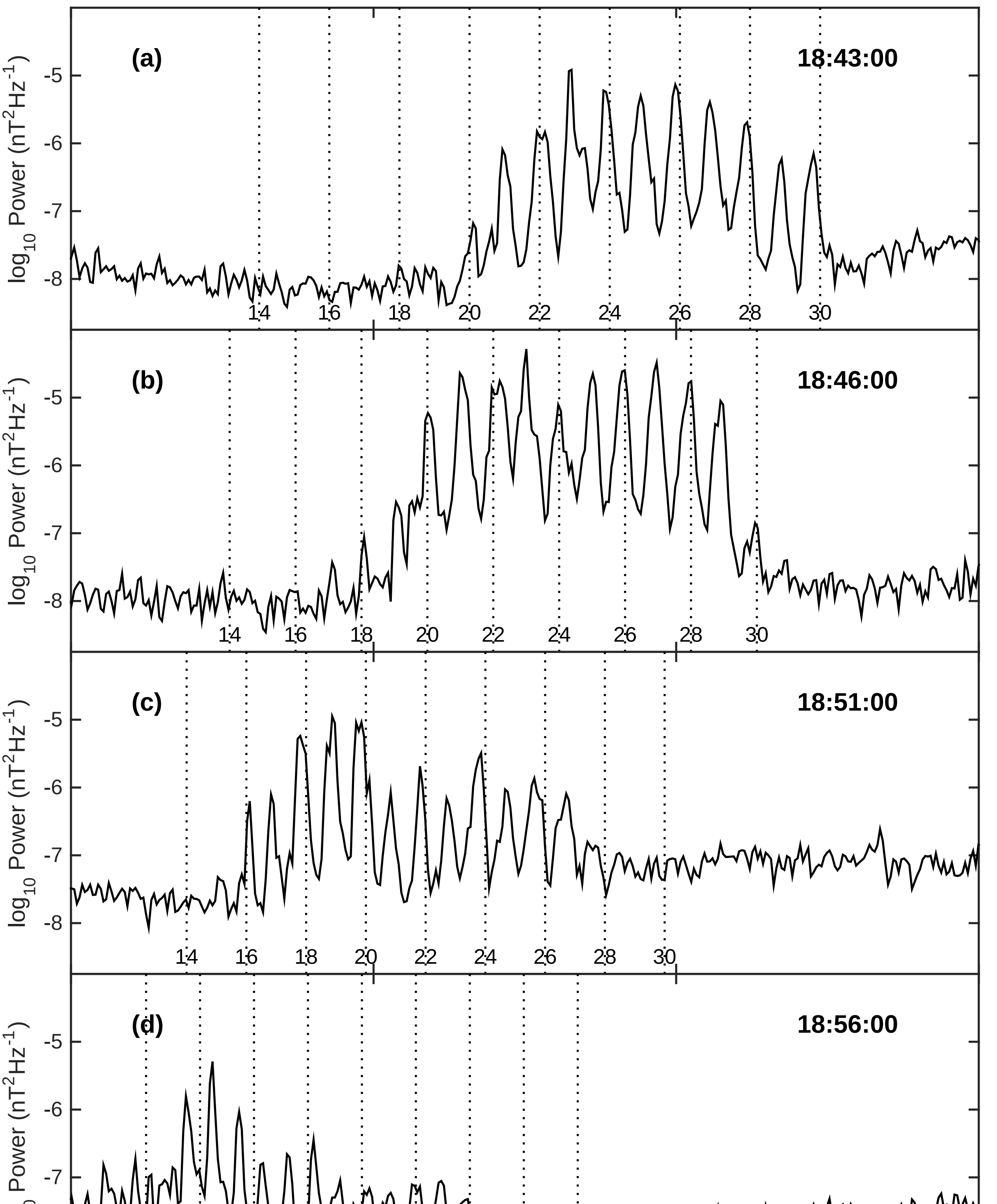
(a)
18:43:00
(b)
18:46:00
(c)
18:51:00
(d)
18:56:00
log$_{10}$ Power (nT^{2}Hz^{-1})
Frequency (Hz)
14
16
18
20
22
24
26
28
30
50
100
150
200
-5
-6
-7
-8

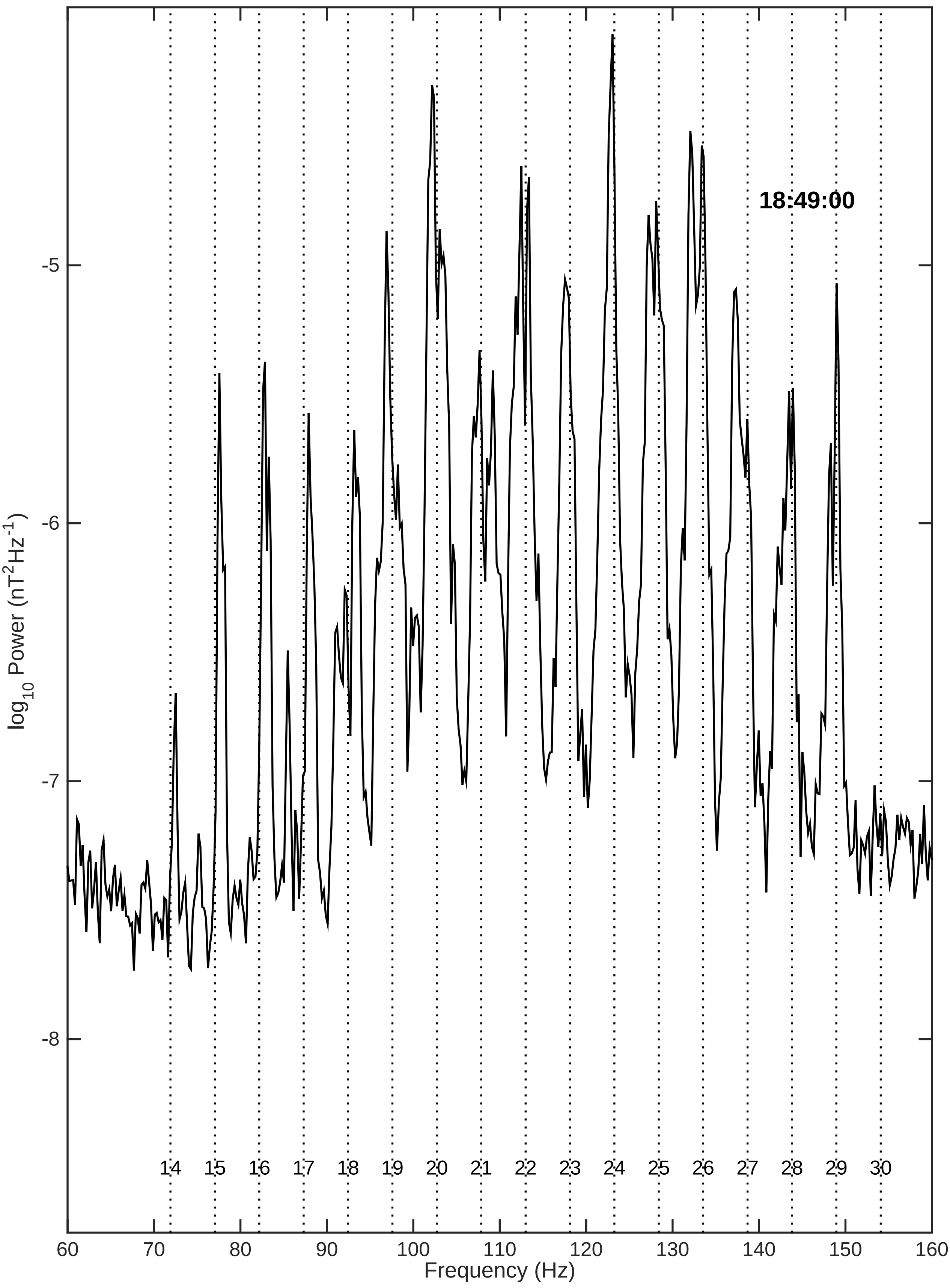

18:49:00
14
15
16
17
18
19
20
21
22
23
24
25
26
27
28
29
30
-5
-6
-7
-8
log10 Power (nT2Hz-1)
60
70
80
90
100
110
120
130
140
150
160
Frequency (Hz)

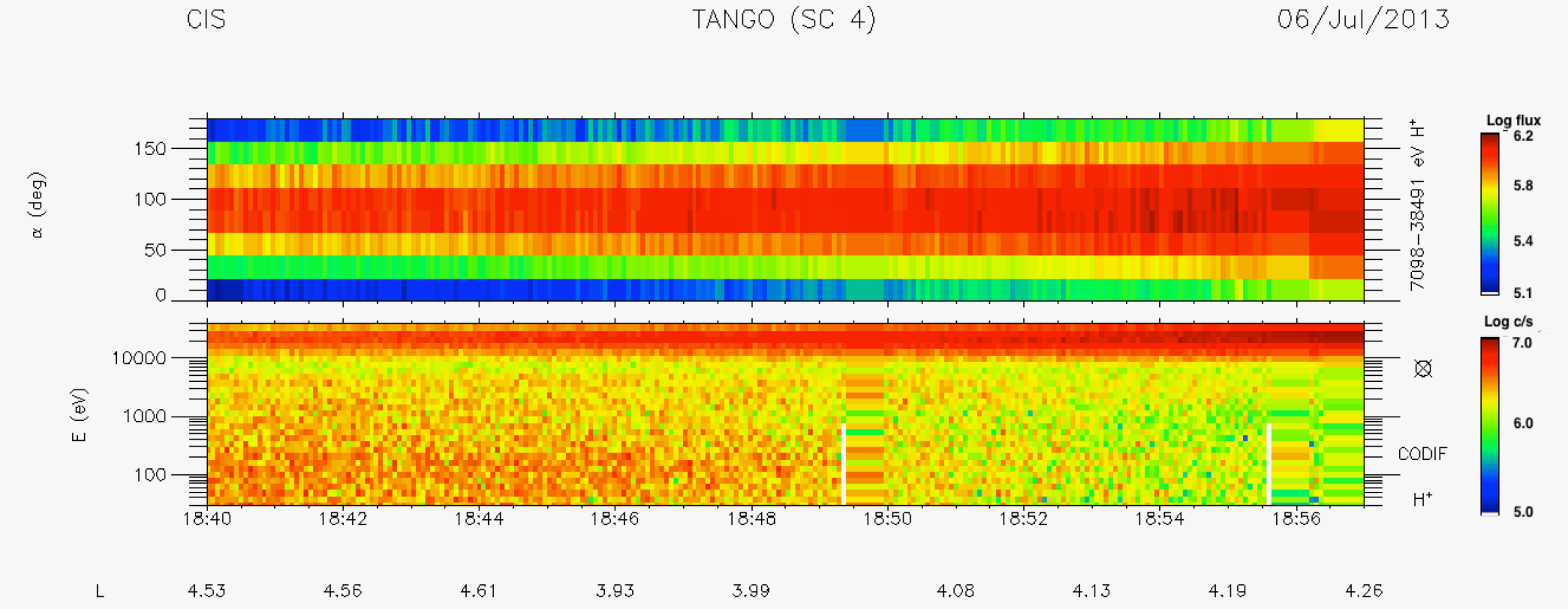

CIS
TANGO (SC 4)
06/Jul/2013
α (deg)
150
100
50
0
7098−38491 eV H+
Log flux
6.2
5.8
5.4
5.1
E (eV)
10000
1000
100
CODIF
H+
Log c/s
7.0
6.0
5.0
18:40
18:42
18:44
18:46
18:48
18:50
18:52
18:54
18:56
L
4.53
4.56
4.61
3.93
3.99
4.08
4.13
4.19
4.26

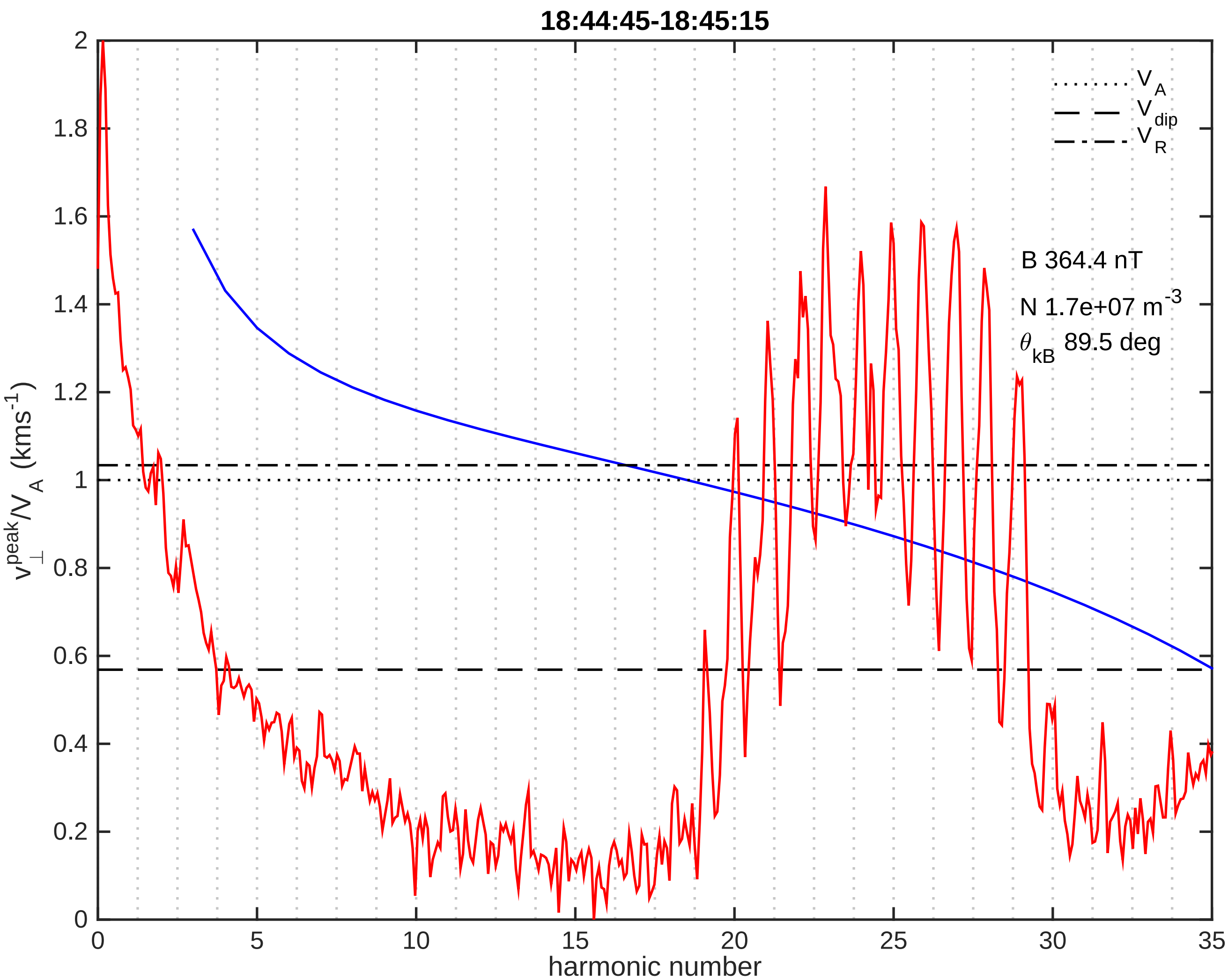

18:44:45-18:45:15
V_A
V_dip
V_R
B 364.4 nT
N 1.7e+07 m^-3
θ_kB 89.5 deg
v_⊥^peak/V_A (kms^-1)
harmonic number

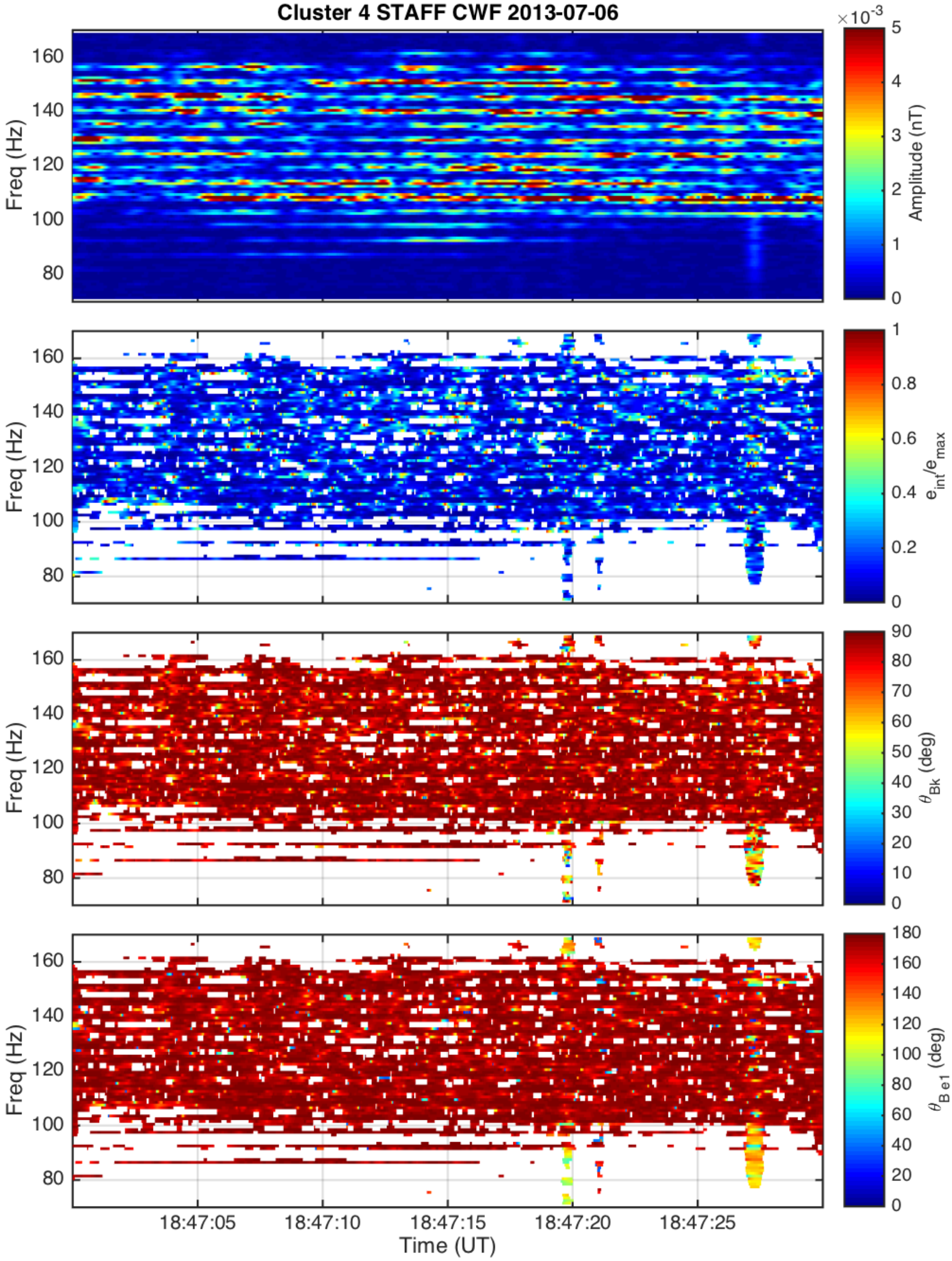
Cluster 4 STAFF CWF 2013-07-06
Freq (Hz)
Amplitude (nT)
×10⁻³
e_{int}/e_{max}
θ_{Bk} (deg)
$\theta_{B\,e1}$ (deg)
18:47:05
18:47:10
18:47:15
18:47:20
18:47:25
Time (UT)

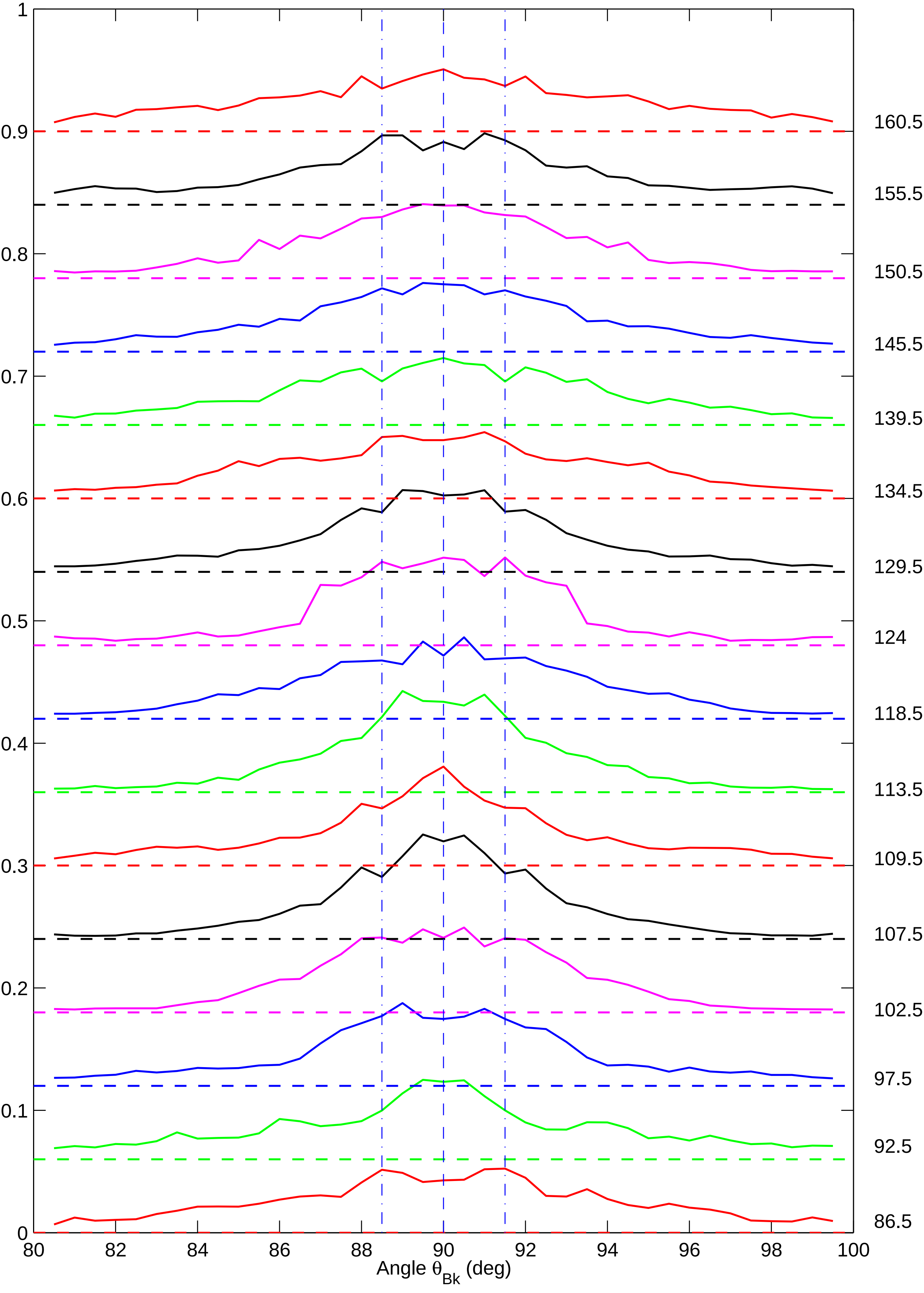

1
0.9
0.8
0.7
0.6
0.5
0.4
0.3
0.2
0.1
0
80
82
84
86
88
90
92
94
96
98
100
Angle θ_{Bk} (deg)
160.5
155.5
150.5
145.5
139.5
134.5
129.5
124
118.5
113.5
109.5
107.5
102.5
97.5
92.5
86.5

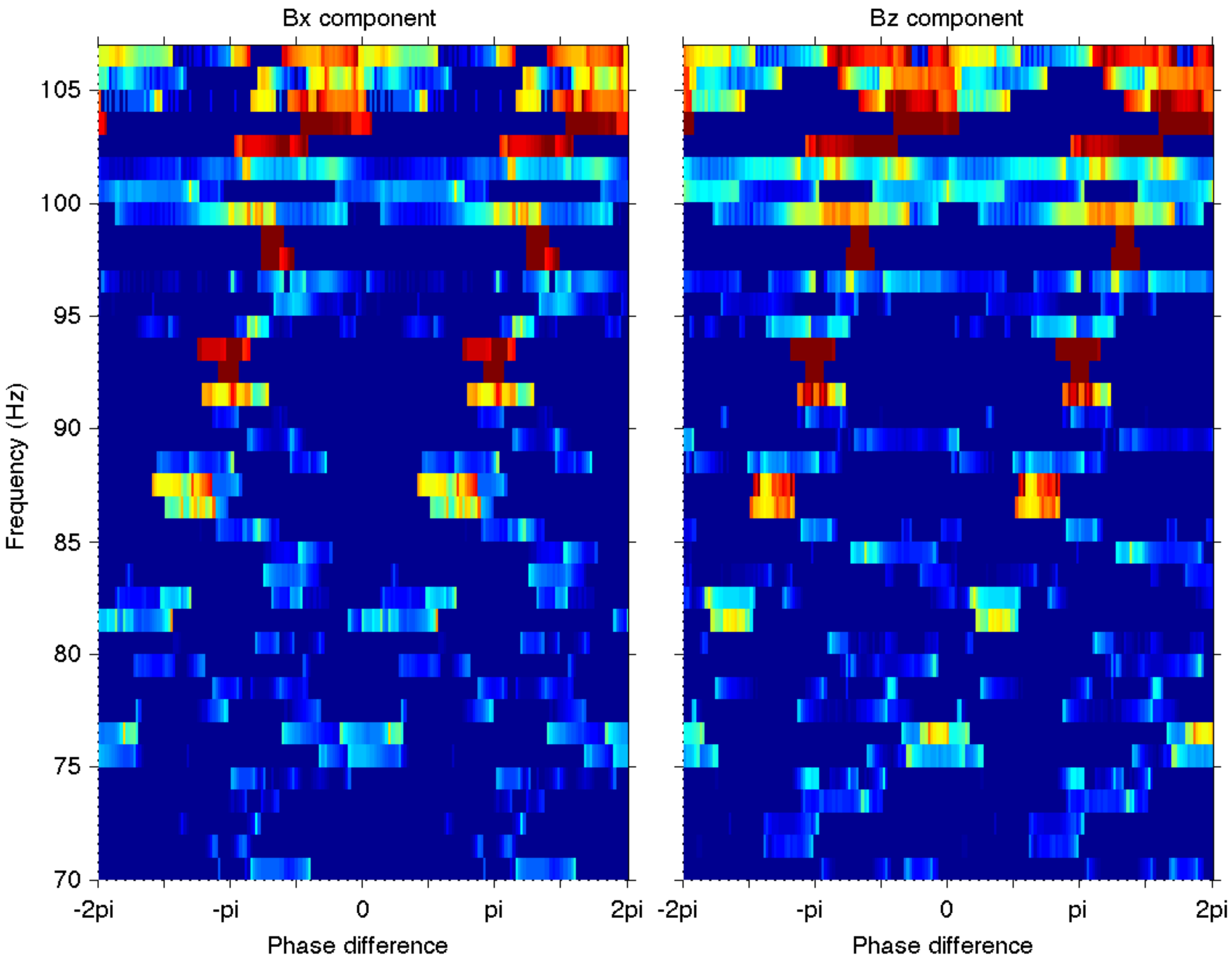
Bx component
Bz component
Frequency (Hz)
105
100
95
90
85
80
75
70
-2pi
-pi
0
pi
2pi
Phase difference

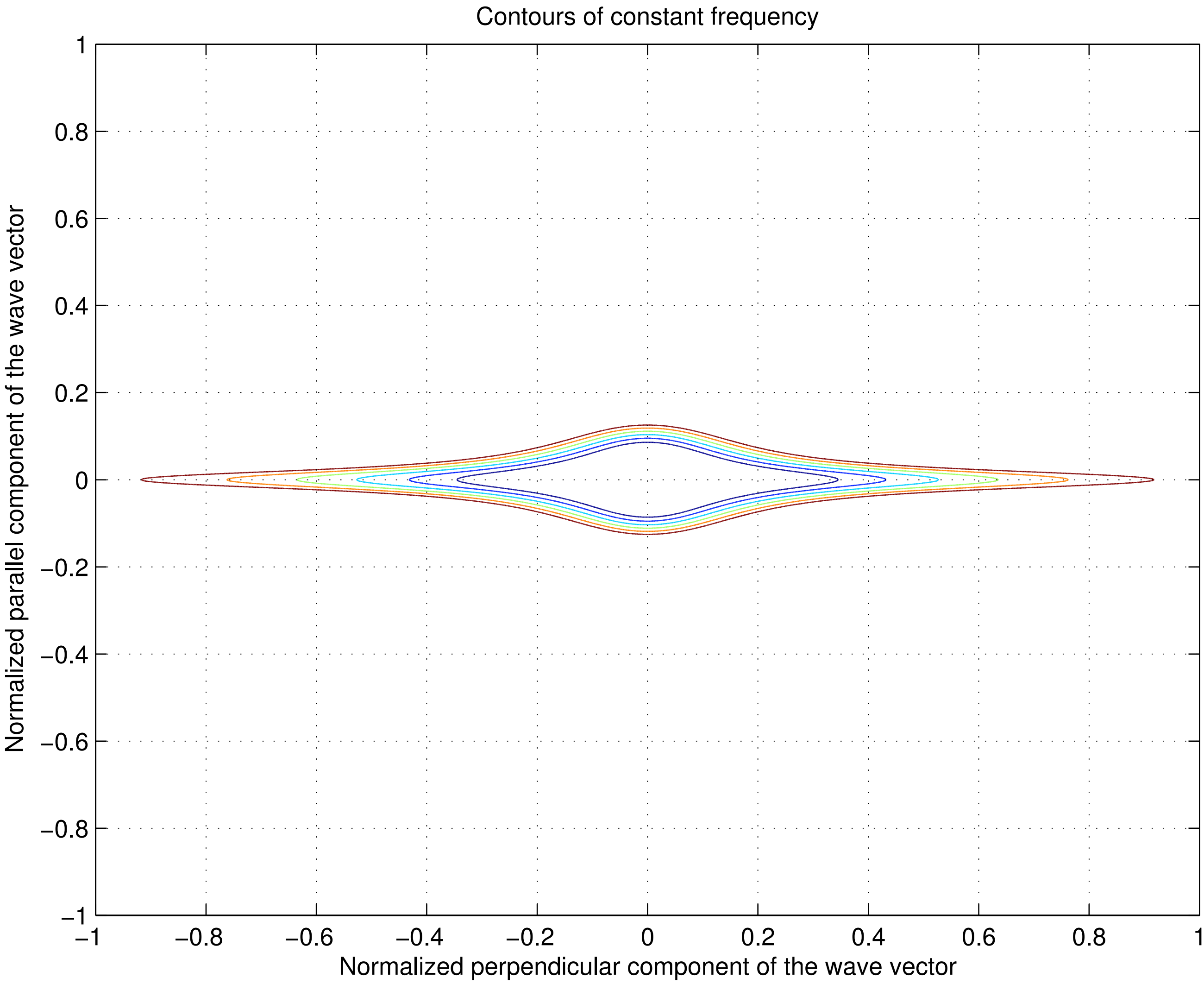

Contours of constant frequency
Normalized parallel component of the wave vector
Normalized perpendicular component of the wave vector
1
0.8
0.6
0.4
0.2
0
−0.2
−0.4
−0.6
−0.8
−1
−1
−0.8
−0.6
−0.4
−0.2
0
0.2
0.4
0.6
0.8
1

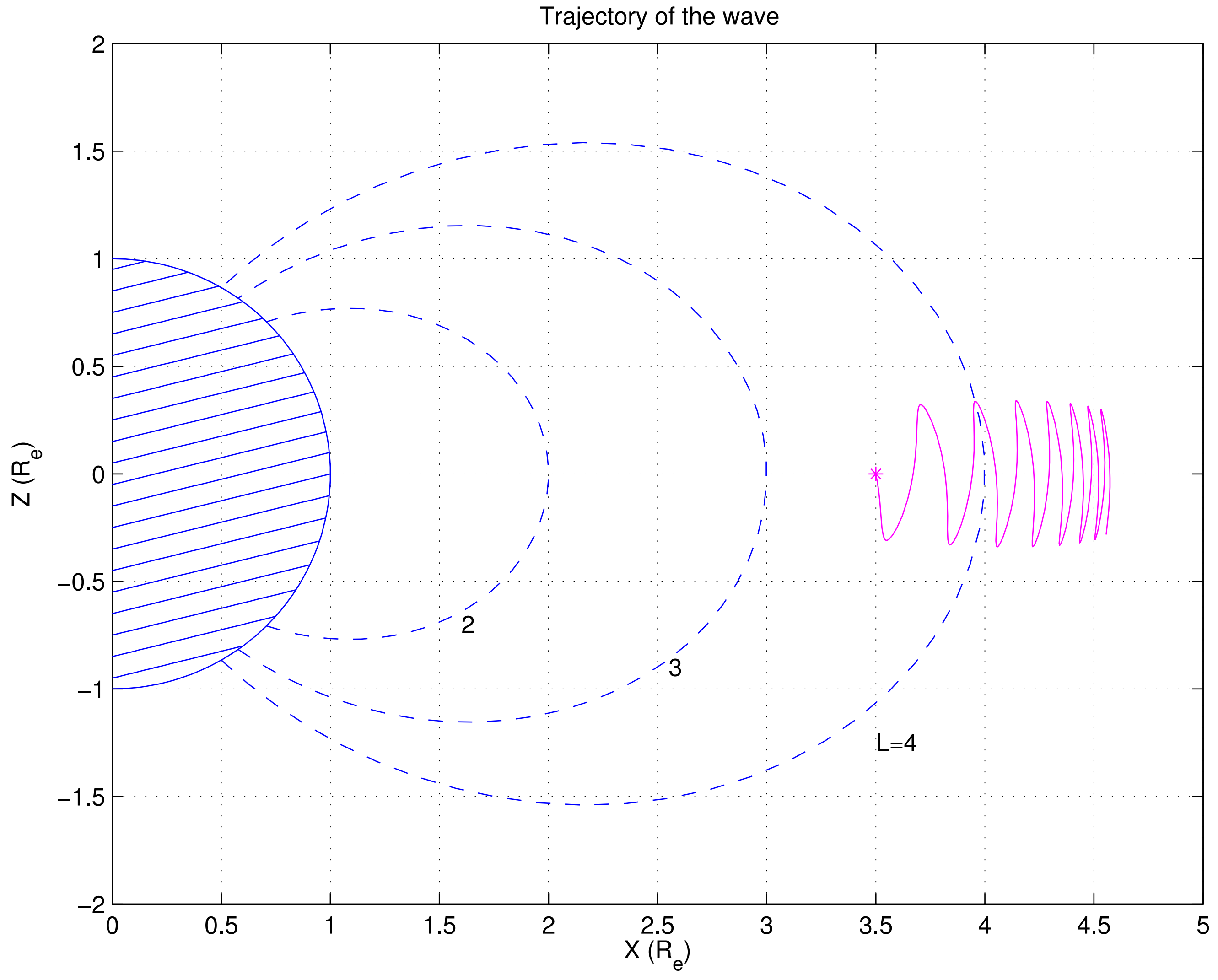

Trajectory of the wave
2
1.5
1
0.5
0
−0.5
−1
−1.5
−2
Z (R_e)
0
0.5
1
1.5
2
2.5
3
3.5
4
4.5
5
X (R_e)
2
3
L=4

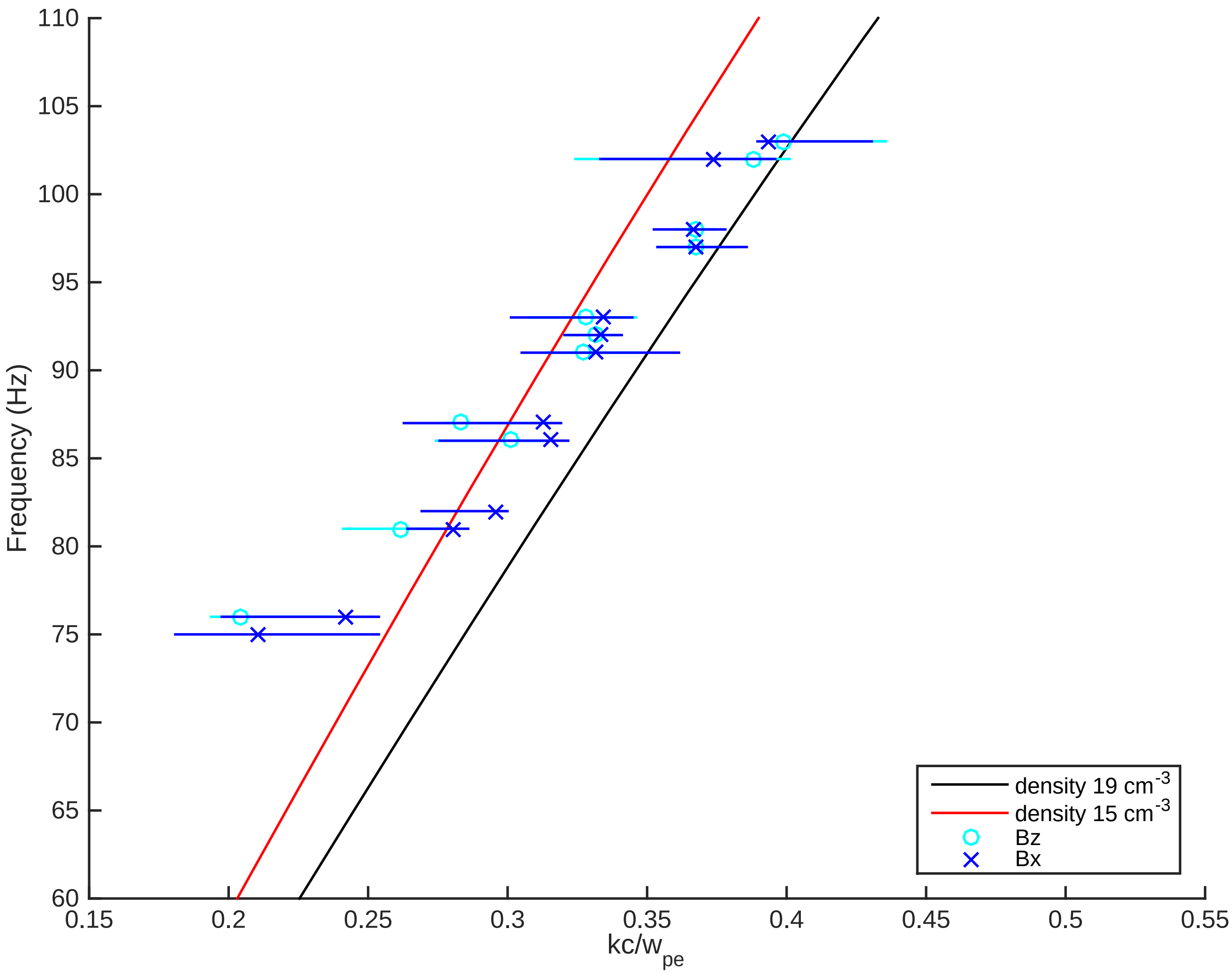

110
105
100
95
90
85
80
75
70
65
60
Frequency (Hz)
0.15
0.2
0.25
0.3
0.35
0.4
0.45
0.5
0.55
kc/w_pe
density 19 cm^-3
density 15 cm^-3
Bz
Bx